Observing the Sun: from start to finish.

PhD dissertation by

Pablo Santamarina Guerrero

Instituto de Astrofísica de Andalucia (IAA-CSIC)

Programa de Doctorado en Física y Matemáticas (FisyMat)
Universidad de Granada

A thesis submitted in fulfillment
of the requirements of the degree of
Doctor of Philosophy

July 26, 2024

PhD thesis supervised by

Dr. David Orozco Suárez
Dr. Julián Blanco Rodríguez

INSTITUTO DE
ASTROFÍSICA DE
ANDALUCÍA

EXCELENCIA
SEVERO
OCHOA

UNIVERSIDAD
DE GRANADA

CONTENTS

CHAPTER 1

TuMag's design and calibration.

In this chapter we take the first steps of the journey of developing an instrument to observe the Sun. We will define...

Fabry-Pérot interferometers (FPIs) are widely employed in the field of solar physics. Their spectroscopic and tunability properties make them especially suitable for selecting a narrow spectral band of incoming light. They also offer a two-dimensional view of the solar scene, hence allowing for the implementation of powerful and widespread image post-processing reconstruction techniques, such as phase diversity (Gonsalves, 1982) and multi-object multi-frame blind deconvolution (MOMFBD; Van Noort et al. 2005), which are difficult to implement in slit-based spectrographs (Noda et al. 2015, van Noort 2017). Many state-of-the-art instruments use FPIs as narrowband tunable filters. Among others, these instruments include the spaceborne Polarimetric and Helioseismic Imager (Solanki et al., 2020) aboard the Solar Orbiter mission (Müller et al., 2020) (SO/PHI); the Imaging Magnetograph Experiment (IMaX) instrument (Martínez Pillet et al., 2011), which flew on the first two flights of the balloon-born SUNRISE observatory (Barthol et al. 2011, Solanki et al. 2017); and the Tunable Magnetograph (TuMag) instrument for its third edition. These instruments are based on solid LiNbO₃ etalons. Regarding ground-based instruments, some examples include the Crisp Imaging Spectro-Polarimeter (CRISP) at the Swedish 1-m Solar telescope (Scharmer et al., 2008) at the Observatorio del Roque de los Muchachos in La Palma, Canary Islands; the GREGOR Fabry-Perot Interferometer (GFPI; Puschmann et al. 2013, Schmidt et al. 2012) at the Observatorio del Teide in Tenerife, Canary Islands; the Visible Tunable Filter (VTF; Schmidt et al., 2016) developed for the *Daniel K. Inouye* Solar Telescope (DKIST; Rimmele et al., 2020) of the Haleakalā Observatory in Hawaii; and the future Tunable Imaging Spectropolarimeter (TIS) of the European Solar Telescope (Noda et al., 2022), all of which are based on air-gapped etalons.

The SUNRISE III mission aims to study and stablish the relations and couplings between the phenomena ocurring at different layers of the Sun's surface. With this purpose in mind, three different post-focal instruments were included in the design, each of them responsible of observing at different regions of the spectrum. The SUNRISE UV Spectropolarimeter and Imager (SUSI, **REFERENCIA**), which will observe the spectra between 309 nm and 417 nm; The Sunrise Chromospheric Infrared spectroPolarimeter (SCIP, **REFERENCIA**), which will observe the near-infrared; and lastly, the Tunable Magnetograph (TuMag), which will ob-

serve three spectral lines in the visible, at 525.02 nm, 525.06 nm and 517 nm.

The design from scratch of an instrument such as this is very complex. There are many things that have to be meticulously designed and tested which span many fields of expertise, like optics, electronics, software, hardware, or thermal design. To avoid undue extension of this thesis, we will focus on the aspects of the design directly related to the **TO QUE**, that is, regarding the spectral, imaging and polarimetric capabilities of the instrument.

1.1 A brief introduction to spectropolarimeters.

Spectropolarimeters, as suggested by the name, are devices that measure the spectral and polarimetric properties of light, or in other words, that measure the polarization state of light as a function of wavelength. Their use is widely extended in astrophysics due to the huge amout of information about the light source we can infer from these properties.

In solar physics, it is common to encounter two distinct types of spectropolarimeters, distinguished by their approach to spectroscopy: slit-based spectrographs, such as SUSI and SCIP, and narrow-band tunable filtergraphs, like TuMag. The latter preserve spatial resolution by capturing two-dimensional images of the solar scene at the expense of sacrificing spectral resolution. Conversely, slit-based spectrographs provide excellent spectral resolution but have a limited spatial resolution.

Regardless of how spectroscopy is carried out, spectropolarimeters must be able to measure the polarization state of light. That is, they must be capable of determining the Stokes parameters of the incident light. These four parameters, usually grouped in a pseudo-vector: $[I, Q, U, V]$, were defined by Stokes in Stokes (1851) as a mathematical formalism to completely define to polarization state of light. The first parameter, I, represents the total intensity; Q and U provide information about the intensity of linearly-polarized light, at 0º and 90º, respectively; and lastly, V, accounts for the intensity of circularly polarized light.

Excellent polarimetric sensitivity and spectral resolution are wasted if the optical capabilities of the instrument are not up to par. The design of these instruments must achieve diffraction-limited imaging, with a signal-to-noise ratio ensuring a polarimetric sensitivity of 1000 (typically), and the best spatial resolution the telescope allows, all without sacrificing spectral resolution and accomplishing this in the shortest possible time.

When designing the instrument, one must balance these three properties: spectral, optical, and polarimetric capabilities, trying to improve the performance in all of them without sacrificing too much. In the following sections, we will delve into each of these aspects in more detail.

1.1.1 Spectroscopy

Narrow-band tunable spectrographs play a significant role in this thesis. They will be extensively discussed in this chapter, particularly in relation to the design and calibration of TuMag, and again in Chapters **??** and 2 when addressing TuMag's pipeline and the correc-

tion of data produced by these instruments. Therefore, for the sake of simplicity, we will focus exclusively on this type of spectrographs from this point onward.

CAMBIAR ESTO.

Fabry-Pérot Interferometers (FPIs), also known as etalons (used interchangeably), represent one of the most prevalent forms of narrow-band tunable spectrographs. Composed by a resonant optical cavity formed by two distinct optical media, these devices allow only the passage of light with wavelengths corresponding to constructive interference within the cavity.

The transmission profile of an etalon, being produced by an interference phenomenon, is characterized by a series of narrow and periodic transmission peaks. The wavelengths at which this resonance peaks are located, their width, and their separation are determined solely by the physical properties of the etalon. In fact, it is not difficult to demonstrate (Bailén et al., 2019a) that a resonant cavity produces a periodic transmission profile, with maxima occurring at a wavelength λ such that:

REVISAR -> VÁLIDO PARA TELECENTRIC??

$$\lambda = \frac{2nd \cos \theta}{m} \; , \tag{1.1}$$

where n is the refractive index of the medium inside the cavity, d is the distance between the mirrors, θ is the angle of incidence of the incoming light ray and m is the interferential order ($m \in \mathbb{Z}$).

With Eq. (1.1) in mind, it is clear that an etalon allows for tuning the wavelengths of the transmission peaks by either changing the distance between the mirrors or by altering the refractive index. Although changing the angle of incidence also results in a wavelength shift, it introduces other issues, such as ghost images or profile broadening in telecentric configurations, among other effects. Consequently, the angle is not used for wavelength tuning.

To tune to a single wavelength (or a very narrow band around it), it is necessary to isolate one transmission peak (main order). This is typically achieved by using a pre-filter that only allows light with wavelengths near the desired measurement region to pass through. This ensures that no light reaches the etalon that could pass through it due to interference orders other than the main one (secondary orders).

Figure 1.1 shows a simulation of the spectral behavior of this optical setup. The order-sorting pre-filter is shown with a shaded purple area and the unaltered transmission profile of the etalon is shown in dahsed lines for different values of the refractive index. In solid lines, the resulting transmission profile is shown, that is, the transmission allowed through both the pre-filter and etalon at the same time.

1.1.2 Polarimetry

As previously noted, determining the polarization state of light requires the determination of the components of the Stokes vector. However, these parameters cannot be measured directly since we only know how to measure intensities. Since they are Thus, measuring the
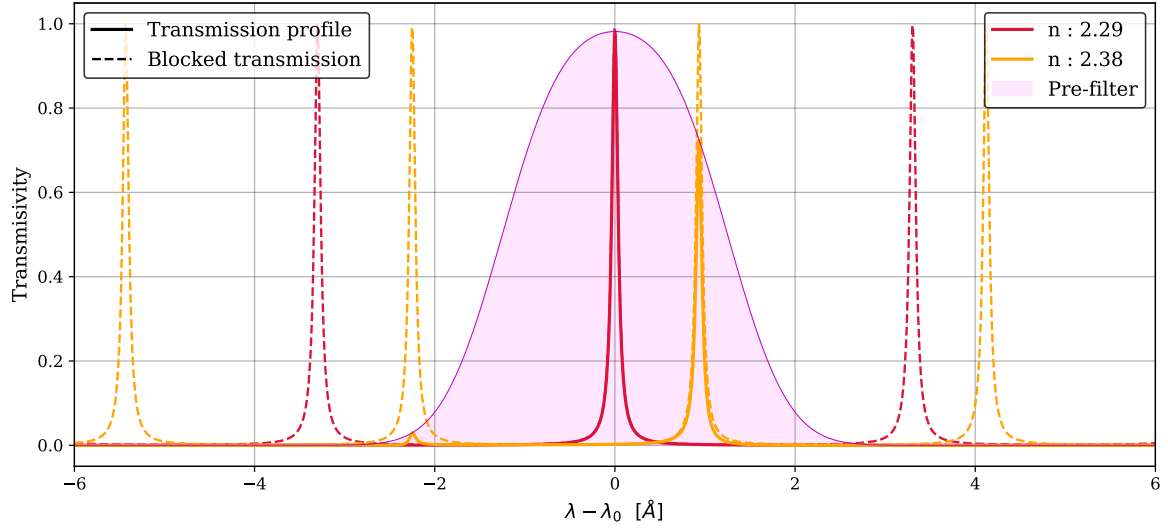
Figure 1.1 Transmission profiles of the same etalon with varying refractive indices (n). The dashed lines represent the original transmission profile, while the solid lines indicate the portion of the transmission profile that passes through the order-sorting pre-filter (shaded purple area).

polarization of light always involves multiple measurements at once. Specifically, a number equal to the number of elements to be determineed: four for the complete Stokes vector, or two, if only the circular polarization and total intensity are to be measured. This is the root of the difficulties in measuring polarization, as the need for multiple measurements makes them much more susceptible to spurious effects compared to individual measurements. Cambiar que es un jaleo.

Mathematically, the effect on polarization of a linear and finite system can be treated as a combination of linear transformations on the Stokes vector and, therefore, can be represented by a matrix in $\mathbb{R}^4$, known as the *Mueller Matrix*. Let **M** be the matrix that describes these transformations, then the polarization state that reaches the detector follows:

$$\mathbf{I}_{out} = \mathbf{M}\mathbf{I}_{in}, \tag{1.2}$$

where $\mathbf{I}_{in}$ and $\mathbf{I}_{out}$ are the Stokes vectors of the light that reaches the instrument, and the detector, respectively. However, since we only know how to measure intensities, the actual quantity measured by our CCD is:

$$I_{obs} = m_{00}I_{in} + m_{01}Q_{in} + m_{02}U_{in} + m_{03}V_{in} \;\;, \tag{1.3}$$

where m_{0i} is the i-th element of the first row of the Mueller Matrix. This means that the intensity we measure is a linear combination of the different polarization states of the incoming light. To determine the values of the individual parameters I_{in}, Q_{in}, U_{in}, and V_{in}, further independent measurements are necessary, which can be achieved by modifying the Mueller matrix. In particular, it is easy to see that four independent measurements are re-

quired in order to construct a system of equations that allows us to determine the full Stokes vector. This process is known as modulation, and the four independent measurements are referred to as modulations.

If we denote each of the modulations by I_j with $j \in \{1, 2, 3, 4\}$, we can construct the following system of equations:

$$\begin{pmatrix} I_1 \\ I_2 \\ I_3 \\ I_4 \end{pmatrix} = \underbrace{\begin{pmatrix} m_{01}^1 & m_{02}^1 & m_{03}^1 & m_{04}^1 \\ m_{01}^2 & m_{02}^2 & m_{03}^2 & m_{04}^2 \\ m_{01}^3 & m_{02}^3 & m_{03}^3 & m_{04}^3 \\ m_{01}^4 & m_{02}^4 & m_{03}^4 & m_{04}^4 \end{pmatrix}}_{\mathbf{O}} \begin{pmatrix} I_{in} \\ U_{in} \\ Q_{in} \\ V_{in} \end{pmatrix} \tag{1.4}$$

where the superindex in m_{oi}^j denotes the values of the Mueller Matrix for each modulation. Through straightforward algebra, it is easy to see that the stokes vector of the incoming light can be determined by $\mathbf{I}_{in} = \mathbf{D}\mathbf{I}_{obs}$, where $\mathbf{D}$ is the demodulation matrix, the inverse of the modulation matrix, $\mathbf{O}$, and $\mathbf{I}_{obs}$ is the vector containing the 4 measured modulations. Accurately determining $\mathbf{O}$ during the instrument calibration process is crucial, as the determination of the Stokes components depends entirely upon it.

1.1.3 Imaging

The high-resolution imaging that etalon-based instruments are capable of is one of the pivotal reasons for their extended use. The ability to capture a two-dimensional scene of the solar surface makes them ideal for studying solar plasma structures, which require resolutions close to 100 km on the solar surface. However, it is essential to achieve these resolutions while maintaining a sufficiently high signal-to-noise ratio to ensure the required polarimetric sensitivity.

Spectropolarimeters ultimately combine measurements in polarization, spectral, and spatial (image) domains. Consequently, the final observed intensity depends on all three properties simultaneously. By integrating the spectral behavior of the etalon and pre-filter with the polatrimetric measurements, and taking into account the spatial dependence of these measurements, the observed intensity for a modulation j at any point of the focal plane η, ξ when the etalon is tuned at a wavelength λ_s is determined by:

$$I_j\left(\xi, \eta; \lambda_s\right) = g(\xi, \eta) \int_0^\infty T(\lambda) \iint O_j\left(\xi_0, \eta_0; \lambda\right) \mathcal{S}\left(\xi_0, \eta_0; \xi, \eta; \lambda - \lambda_s\right) \mathrm{d}\xi_0 \, \mathrm{d}\eta_0 \mathrm{d}\lambda,$$
$$\tag{1.5}$$

where $T(\lambda)$ accounts for the presence of the order-sorting pre-filter, $\mathcal{S}\left(\xi_0, \eta_0; \xi, \eta; \lambda - \lambda_s\right)$ accounts for the imaging response of the instrument when tuned at the wavelength λ_s, $g(\xi, \eta)$ represents a spatial gain factor that accounts for any wavelength independent pixel-to-pixel intensity fluctuations ocurring in the focal plane, and $O_j(\xi_0, \eta_0; \lambda)$ is the intensity

distribution of the incoming light for a modulation j and is given by:

$$O_j(\xi_0, \eta_0; \lambda) = m^j_{00} I_{in}(\xi_0, \eta_0; \lambda) + m^j_{01} Q_{in}(\xi_0, \eta_0; \lambda) + m^j_{02} U_{in}(\xi_0, \eta_0; \lambda) + m^j_{03} V_{in}(\xi_0, \eta_0; \lambda)$$
(1.6)

Determining the imaging response of the instrument can be quite complex , as it is influenced not only by their physical characteristics but also by their optical configuration, whether collimated or telecentric. In Chapter 2, we provide a detailed overview of the properties of each configuration, their differences, and the challenges involved in using these devices for data correction.

ADD noise Discussion?

1.1.4   What do spectrpolarimeters tell us about the Sun?

Spectropolarimeters are often referred to as magnetographs (*e.g.*, TuMag), suggesting they measure magnetic fields directly. However, this is not entirely accurate. In astrophysics, the physical properties of the light source are inferred by correlating them with the observed properties of the light, rather than measuring them directly. By evaluating the polarization of sunlight at different wavelengths, spectropolarimeters enable us to infer the magnetic field and estimate plasma velocities on the solar surface.

The simplest calculation we can carry out that provides us with physical quantities of the Sun is that of the line-of-sight (LOS) velocities. Given the spectral shift of a specific absorption or emission spectral line, $\Delta\lambda$, with respect to its rest position, λ_0 , the LOS velocities can be computed with the Doppler formula:

$$v_{LOS} = \frac{\Delta\lambda}{\lambda_0} c \ ,$$
(1.7)

where c stands for the speed of light in vacuum.

The polarization properties of light come into play when determining the magnetic fields. Due to Zeeman and Hanle effects, the polarity and spectcroscopy of spectral lines can be altered when formed in the presence of magnetic fields. Due to the Zeeman effect, the spectral lines widen or split into different polarized components when a strong magnetic field is present (del Toro Iniesta, 2003), such as in the surroundings of sunspots and active regions. In the other hand, the Hanle effect is sensitive to weaker fields, and can be used to study the magnetic structure of solar prominences or turbulent fields in the solar photosphere (Bianda et al., 1998).

One simple strategy to employ polarization and spectral data to derive the magnetic fields is through the center-of-gravity method. According to Uitenbroek (2003), the LOS strength of the magnetic field can be obtained through:

$$B_{LOS} = \frac{\lambda_+ - \lambda_-}{2} \frac{4\pi mc}{e \, g_L \lambda_0^2} \ ,$$
(1.8)

where m and e are the electron mass and charge respectively, g_L stands for the Landé factor and λ_+ and λ_- are the centroids of the right and left circularly polarized line components,

respectively, and are computed by:

$$\lambda_{\pm} = \frac{\int \lambda \left[I_{cont} - (I \pm V) \right] d\lambda}{\int \left[I_{cont} - (I \pm V) \right] d\lambda} \ , \tag{1.9}$$

where the subindex "$cont$" stands for the wavelength at the continuum. The vector magnetic field (*i.e.*, strength, azimuth and inclination), and not only the LOS strength can also be derived. However, the derivation of these quantities has to be achieved through inversions of the radiative transfer equation (RTE). The applicability of the different methods to carry out this inversion is an extensive topic as there are some assumptions that can be applied in some cases but not in others, such as the weak-field or Milne-Eddington approximations, among others. For an extended discussion of this topic, we refer the interested reader to del Toro Iniesta & Ruiz Cobo (2016).

1.2 The Tunable magnetograph: TuMag

Among many examples of spectropolarimeters, one that has special relevance for this thesis is TuMag. The Tunable magnetograph (TuMag) is a wavelength-tunable spectropolarimeter that observes in the photosphere and the low chromosphere.

TuMag is a filtergraph that employs a solid LiNbO$_3$-based FPI to scan the spectral lines. This kind of etalons are able to change the refractive index of the matierial inside the cavity by applying a voltage difference between the two mirrors. This design advantageously eliminates moving parts from the tuning process, though it requires high voltages for operation.

In order to be able to carry out observations of both the photosphere and low cromosphere, TuMag must be able to switch between different spectral lines. For this purpose, TuMag is equipped with three different pre-filters centered at the wavelengths of three different spectral lines: The FeI line at 5250.2 Å, the FeI line at 5250.6 Å, and the Mg line at 5172.7 Å.

1.3 Calibration of TuMag

CHAPTER 2

CHALLENGES IN DATA REDUCTION.

ETALON CAVITY MAP

Thus far, we have focused on TuMag, its properties, and the correction of its data due to its central role in this thesis. However, other tunable magnetographs exist, each with its own specific characteristics, advantages, and challenges. In this chapter, we shift our focus away from TuMag (partially) and turn our attention to another class of magnetographs, specifically those with their etalon in a telecentric configuration.

Currently, there is an ongoing debate within the scientific community regarding the optimal optical configuration for an etalon, whether it should be collimated or telecentric. This debate has garnered significant interest, as evidenced by the numerous studies addressing the properties of each configuration. Notable contributions include the four works by Bailén et al. (Bailén et al. 2019a, Bailén et al. 2019b, Bailén et al. 2020, Bailén et al. 2021), which offer an extensive analysis on topics such as the impact of defects, applications for instrumentation, and the analytical formulation of the etalon's transmission profiles. Other examples include the studies by (Beckers, 1998) and (Scharmer, 2006), which analyze the optical performance of FPIs, as well as the works of Kentischer et al. 1998 and Cavallini 2006, which discuss the properties of the etalons in the Telecentric Etalon Solar Spectropolarimeter (TESOS) and the Interferometric BIdimensional Spectrometer (IBIS), respectively. Additionally, the review of Bailén et al. 2023 provides a broad and comprehensive overview of this topic. The reality is that it is challenging to provide a definitive answer to this question, as each configuration has its own advantages and disadvantages.

The primary argument against collimated mounts is the amplification of wavefront errors resulting from the large footprint of the light rays on the etalon plates, which encompasses both large and small scale defects (Bailén et al., 2023). This amplification deteriorates the optical quality of these setups and has promoted the use of telecentric setups, where the footprints of the light rays are much smaller and the optical performance is less affected by large scale defects.

Despite its potential benefits, the telecentric configuration is no exempt of challenges. In this configuration each light ray trasverses the etalon through different regions, thus

being affected differently at each point from the various small scale defects present in the etalon. This defects, compose the so-calleed, cavity-map and its correction can be one of the main challenges of employing this setups.

This chapter aims to provide a comprehensive examination of telecentric configurations for etalons within the context of solar spectropolarimeters. We will begin by exploring the analytical formulation of the transmission profiles and spatial PSF of FPI's in both collimated and telecentric configurations. Following this, we will delve into the effects of the cavity error in solar observations, and the strategies employed to mitigate its effects, through a simulation of an observation of a Sunspot. Then, we will present a strategy to derive the cavity map from flat field observations in an attempt to improve the data correction. This strategy is presented and tested in a forthcoming academic paper under the title of "Correcting Fabry-Perot etalon effects in solar observations" [1], and the contents of the corresponding section will be extracted from there.

2.1   One device, two configurations.

We established in section 1.1.3 that the observed intensity distribution at the coordinates ξ, η of the focal plane of any etalon-based instrument tuned to a wavelength λ_s obeys the following expression (Bailén et al., 2019a):

$$I\left(\xi, \eta; \lambda_s\right) = g(\xi, \eta) \int_0^\infty T(\lambda) \iint O\left(\xi_0, \eta_0; \lambda\right) \mathcal{S}\left(\xi_0, \eta_0; \xi, \eta; \lambda - \lambda_s\right) d\xi_0 \, d\eta_0 d\lambda, \quad (2.1)$$

where $T(\lambda)$ accounts for the presence of an order-sorting pre-filter, $O\left(\xi_0, \eta_0; \lambda\right)$ represents the brightness distribution of the observed object at the point $\left(\xi_0, \eta_0\right)$, $S\left(\xi_0, \eta_0; \xi, \eta; \lambda - \lambda_s\right)$ accounts for the imaging response of the instrument when tuned at the wavelength λ_s, and $g(\xi, \eta)$ represents a spatial gain factor that accounts for wavelength independent pixel-to-pixel intensity fluctuations ocurring in the focal plane due to differences in the detectors' sensitivity.

The imaging response of the instrument coincides with the PSF of the instrument when the optical response is invariant against translations. In such a case, we can substitute the last two integrals by the convolution operator, but this is not strictly true in etalon-based instruments, where the response varies pixel to pixel either because of etalon irregularities or because of variations in the illumination across its clear aperture.

Deriving S typically requires determining the electric field of the polychromatic wave in the image plane. According to Bailén et al. (2019a), this field can be calculated by summing all the electric fields ($E^{(t)}$) across the pupil, such that the eletric field at any point (ξ, η) of the image plane follows the expression:

$$E_{im}^{(t)}(\xi, \eta) = \frac{1}{\pi R_{pup}^2} \int \int_{pupil} E^{(t)}(x, y) e^{-ik(\xi x/f + \eta y/f) dx dy}, \quad (2.2)$$
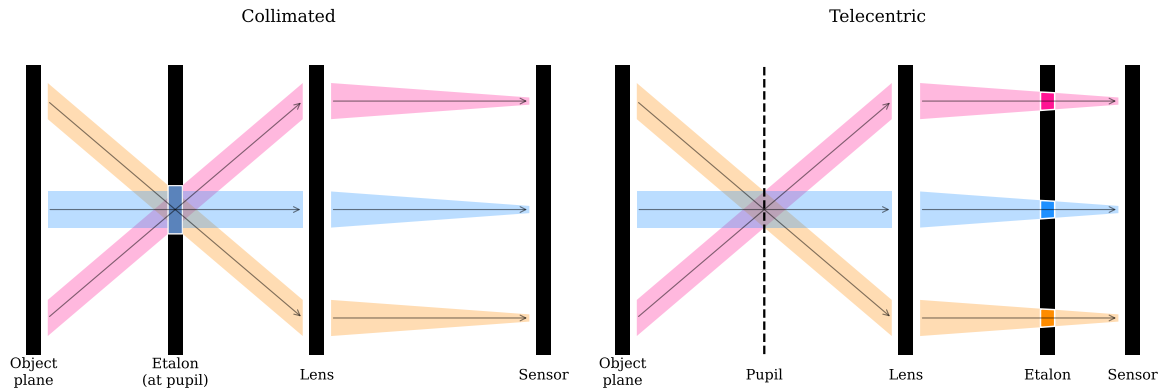
Figure 2.1 Schematic representation of the two optical setups of an FPI, collimated (left) and telecentric (right). The different colors represent distinct light rays originating from various points on the object plane. The white boxes in the etalon highlight the sections that are traversed by the light rays.

where (x, y) are the coordinates in the pupil, f stands for the focal length, and R_{pup} is the radius of the pupil. It can also be shown that the vector electric fields transmitted by the etalon can be expressed as:

$$E^{(t)}(\xi, \eta) = \frac{\sqrt{\tau}}{1 - R} \frac{e^{i\delta/2} - Re^{-i\delta/2}}{1 + F \sin^2(\delta/2)} E^{(i)},$$ (2.3)

where τ is the transmission factor for normal incidence, R stands for the reflectivity of the etalon mirrors, F is a factor defined as $F \equiv 4R(1 - R)^{-2}$, $E^{(i)}$ are the incident electric fields, and δ stands for the phase differences between the transmitted and incident rays.

The transmission profile of the etalon (S) is defined as the average ratio between the transmitted and incident intensities, calculated from the complex conjugate of the corresponding electric fields. The shape of δ varies depending on the illumination setup of the etalon, whether collimated or telecentric. Consequently, each configuration has unique solutions and characteristics and is differently affected by inhomogeneities (defects) in the etalon's properties.

2.1.1 Collimated configuration

Collimated mounts are characterized by having the etalon located at the pupil plane and therefore receive a collimated beam from each point of the observed object. As illustrated in the schematic on the left side of fig. 2.1, light from any point on the object will fall on the same area of the etalon. Consequently, any local defects on the etalon crystals or on the plates' parallelism is averaged all over the clear aperture, thus making the optical quality constant along the FoV. However, the angle of incidence of the light beam varies along the FoV, thus shifting the spectral transmission profile.

Analytical solutions of equation (2.2) are imposible to obtain if δ has a dependence on

the pupil coordinates, as is the case of collimated etalons with a presence of local defects. In that case, the transmssion profile of the etalon has to be evaluated numerically.

However, in order to study the spectral behavior of the transmission profile, we can, as a first-order approximation, disregard the spatial PSF and focus solely on the spectral transmission profile (ψ). Under this assumption, the phase difference between the incident and transmitted rays of an ideal collimated etalon can be expressed as:

$$\delta(\xi, \eta, \lambda) = \frac{4\pi}{\lambda} nd \cos(\theta(\xi, \eta)), \tag{2.4}$$

where n stands for the refractive index of the etalon cavity, d is the distance between the mirrors and θ is the angle of incidence. In such a case, it can be shown that the spectral transmission profile follows the expression:

$$\psi\left(\xi, \eta, \lambda\right) = \frac{\tau}{1 + F \sin^2(\delta(\xi, \eta, \lambda)/2)}. \tag{2.5}$$

The spectral behaviour of the transmission profile, such as the spectral position of the resonance peaks and the distance between them (the free spectral range), is encoded in the parameter δ, which is a function of the refractive index of the etalon cavity, the distance between mirrors, and the angle of the incident beam. The reflectivity R of the mirrors determines the width of the resonance peaks through the parameter F, $F \equiv 4R(1 - R)^{-2}$.

Local defects in the collimated configuration are averaged out, which means that d and n respectively represent the mean values of the thickness and refractive index across the clear aperture of the FPI, and thus remain constant for every pixel. Yet, they produce a broadening of the transmission profile and worsen the optical quality of the instrument. However, the spatial dependence of ψ naturally arises from θ, which vcaries from pixel to pixel.

Assessing the spatial PSF of the FPI is more challenging, as it can only be determined analytically for monochromatic light and in the absence of defects. We will not delve into the equations for this specific scenario as it lies beyond the scope of this thesis. However, interested readers are referred to the work of Bailén et al. (2019a), where this topic is extensively discussed.

2.1.2   Telecentric configuration

In the telecentric configuration, the etalon is placed very close to an intermediate focal plane, while the pupil is focused at infinity. As shown in the sketch on the right side of fig. 2.1, in this setup, the etalon is illuminated by cones of rays that are parallel to each other, thus passing through different sections of the interferometer. Local inhomogeneities (defects or cavities) on the etalon produce differences in the transmission profile across the FoV, which are directly mapped into the image plane. This means that the optical response and the transmission profile shift locally on the image sensor.

In telecentric configurations, δ always depends on the coordinates of the pupil, even in the absence of defects, since each point in the etaon sees a cone of rays coming from dif-

ferent parts of the pupil. Thus, as stated before, solutions to equation (2.2) are to be found numerically. Nonetheless, if we neglect the spatial PSF once again, we can derive an analytical expression for an ideal telecentric etalon, where all light cones impact perpendicularly.

After some messy algebra and clever variable changes, one can recast eq. (2.2) in terms of the radial coordinates of the pupil and anallytically solve the equations. The resulting spectral transmission profile of an ideal telecentric etalon is given by (Bailén et al., 2021):

$$\Psi\left(\xi, \eta, \lambda\right) = \Re\left[E(a\left(\xi, \eta, \lambda\right), b\left(\xi, \eta, \lambda\right))\right]^2 + \Im\left[E(a\left(\xi, \eta, \lambda\right), b\left(\xi, \eta, \lambda\right))\right]^2, \quad (2.6)$$

with $E(a\left(\xi, \eta, \lambda\right), b\left(\xi, \eta\right))$ being:

$$E(a\left(\xi, \eta, \lambda\right), b\left(\xi, \eta\right)) = 2\sqrt{\tau}\left\{\frac{1}{\alpha_1}\left[\arctan(\gamma_1) - \arctan(\gamma_2)\right] +\right.$$

$$\left. i\frac{1+R}{1-R}\frac{1}{\alpha_2}\left[\ln\left(\frac{(1+\gamma_3)^2 + \gamma_4^2}{(1-\gamma_3)^2 + \gamma_4^2}\right) - \ln\left(\frac{(1+\gamma_3)^2 + \gamma_5^2}{(1-\gamma_3)^2 + \gamma_5^2}\right)\right]\right\}, \quad (2.7)$$

where, the auxiliary functions are defined as:

$$a\left(\xi, \eta, \lambda\right) \equiv \frac{2\pi}{\lambda}n\left(\xi, \eta\right)d\left(\xi, \eta\right),$$

$$b\left(\xi, \eta\right) \equiv \frac{1}{8n\left(\xi, \eta\right)^2 (f\#)^2},$$

$$\alpha_1 \equiv 2ab\sqrt{F},$$

$$\alpha_2 \equiv 2\alpha_1\sqrt{F+1},$$

$$\gamma_1 \equiv \sqrt{F}\sin a,$$

$$\gamma_2 \equiv \sqrt{F}\sin(a[1-b]),$$

$$\gamma_3 \equiv \sqrt{\frac{F}{F+1}},$$

$$\gamma_4 \equiv \frac{\tan\left(a/2[1-b]\right)}{\sqrt{F+1}},$$

$$\gamma_5 \equiv \frac{\tan(a/2)}{\sqrt{F+1}}.$$

$$(2.8)$$

The parameter a has the same role as δ for the collimated case. However, the dependence on the image plane coordinates in this case is caused by potential variations in n and/or d, as each light beam traverses different sections of the etalon. These variations constitute the "cavity map" of a telecentric etalon and must always be taken into account during data reduction processes.

The parameter b accounts for the contribution of the focal ratio, $f\#$, and has an impact on the spectral resolution and the apodization of the pupil as seen from the etalon (Beckers, 1998). Thus, the resolution is now affected by both F and $f\#$, through the parameters a and b.
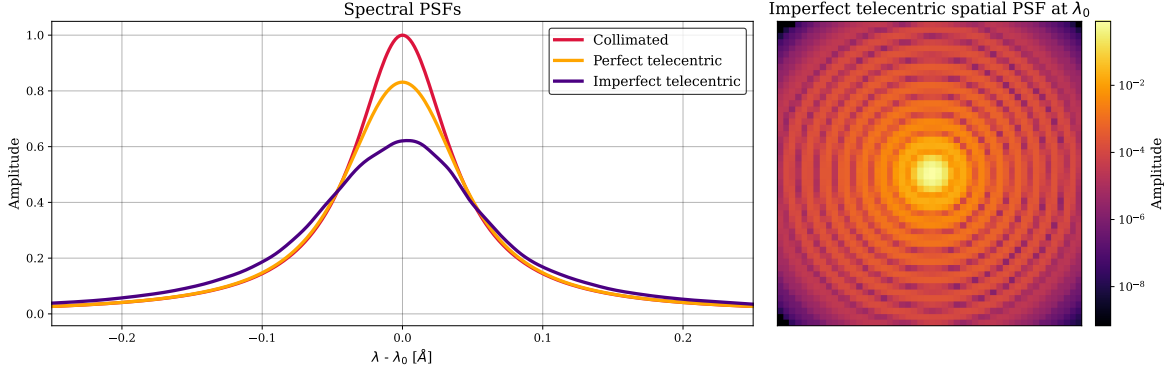
Figure 2.2 *Left*: central peak of the etalon's spectral transmission profile for the three different configurations. *Right*: Spatial PSF of the imperfect telecentric etalon at λ_0. The parameters of the etalon are $R = 0.92$, $n = 2.29$, $d = 251\,\mu$m, $f\# = 56$, $\theta = 0°$ (collimated and perfect telecentric), and $\Theta = 0.3°$ (imperfect telecentric).

2.1.2.1   Telecentric imperfect configuration

The equations shown in Sect. 2.1.2 are valid whenever the incident cone of rays is perpendicular to the etalon mirrors. We refer to this situation hereinafter as "perfect telecentrism". However, real instruments are likely to present deviations from such an ideal case. These deviations can be caused by an intentional tilt of the etalon to suppress ghost images on the detector (Scharmer, 2006), by an accidental tilted angle of incidence caused by deviations from the ideal paraxial propagation of rays within the instrument, or simply because of misalignment of the optical components. In the three cases, the incident cone of rays is no longer perpendicular to the etalon, and hence, we consider these scenarios to have imperfections in the telecentrism degree. One important consequence of the loss of telecentrism is an asymmetrization of the transmission profile that must be accounted for when modeling the instrument response.

The transmission profile in this case is influenced by the angle of incidence of the chief ray at each point of the clear aperture of the etalon, in addition to the parameters mentioned in the previous sections. Unfortunately, the equations for the transmission profile in these configurations are much more complicated than in the ideal case, and can no longer be anallytically solved. We must revisit equation (2.2) and solve the integrals numerically.

Figure 2.2 shows on the left the transmission profile corresponding to the three different scenarios: collimated illumination of the etalon, perfect telecentrism, and imperfect telecentrism. The etalon parameters have been selected to coincide with those of SO/PHI's etalon. In both the collimated and perfect telecentric configurations, a normal incidence ($\theta = 0$) scenario is shown, whereas in the imperfect telecentric case, we assumed an angle of incidence of the chief ray, Θ, of $0.3°$. The parameter a has been adjusted slightly in order to tune the transmission profile at λ_0.

Regarding the properties of each profile, note that the telecentric configurations achieve lower peak transmissions than the collimated case. In addition, the telecentric profiles are wider due to the different incidence angles across the illuminating cone of rays. Such a

broadening increases with decreasing f-ratios. Lastly, non-normal incidence of the chief ray in the telecentric configuration further widens and shifts ($\sim$ 4 mÅ for $\Theta = 0.3°$) the profile, making it asymmetrical.

2.2   Sunspot observation simulation

The analytical formulations equip us with the tools necessary to investigate the impact of the cavity map on observational data and the consequences of incorrect or incomplete corrections. To this end, we will simulate a series of observations of a sunspot using a telecentric FPI and attempt to correct the observations utilizing generated flat-fields. Our aim is to quantify the spurious effects of the cavity map on scientific products, specifically the line-of-sight (LOS) velocities and magnetic field strength.

We have chosen to employ a sunspot for this study since they are one of our main *laboratories* for the study of the magnetic field and dynamics of the solar photosphere. Sunspots are dark regions of the solar surface where strong magnetic fields gather. The innermost part of the spot, the umbra, with a brightness around the 20% of its surroundings, hosts very strong magnetic fields oriented almost perpendicular to the solar's surface. Surrounding the umbra in fully developed sunspots is the penumbra, a brighter region characterized by a radial filamentary structure with a nearly horizontal outflow of the plasma known as the Evershed flow (Evershed, 1909).

The physical mechanisms driving the phenomena in these regions are not yet fully understood and have been a topic of discussion for many years. Processes such as the Evershed flow lack a universally accepted theoretical model, and numerous studies attempt to provide a theoretical basis for the observations, often presenting conflicting interpretations. Some examples of these works are (Schlichenmaier et al., 1998), or (Solanki & Montavon, 1993), where they interpret the evershed flow as a hot gas confined to magnetic flux tubes that rises due to convecion processes; other models, such a the ones proposed by Scharmer & Spruit 2006 and Spruit & Scharmer 2006, suggest that filaments are field-free gaps where regular convection takes place. These convective cells are elongated when the upflow is deflected by the inclined magnetic field, characteristic of the penumbra, thus generating the outward flow.

The optical and spectral properties of the FPIs are fully dependent on the etalon's physical attributes. In particular, the position and width of their resonance peaks vary with the reflectivity, distance between mirrors, refractive index, and angle of the incident beam. Any small and local variation of these parameters with respect to the nominal values alters the transmission profile, shifting it in wavelength and/or widening the bandpass. Such deviations across the clear aperture of the etalon also have a very strong impact on the imaging quality of the instrument (Scharmer 2006, Bailén et al. 2021). It is therefore crucial to characterize how different deviations in the interferometer's physical properties affect the transmission profile and the resulting image quality in order to be able to correct the data for any of these effects.

Artifacts such as the ones originating from pixel-to-pixel differences in the sensitivity of

the detector, instrumental artificial intensity gradients, bright spots, or interference fringe patterns, among others, are corrected via data flat fielding. A flat-field image is built by averaging many images taken with homogeneous illumination or, in the case of solar physics, by averaging many images taken over a region without solar activity, that is, without active regions while continuously moving the telescope to different positions. This way, flat fields can measure the effect of all defects mentioned above. In instruments with FPIs in telecentric configurations, it is not possible to fully reproduce the same illumination, and therefore after the flat-field correction, second-order residuals are expected.

INTRO sunspot. Challenges in data reduction, unknown effects etc.

2.2.1   Simulated data.

MHD? From where.

In order to obtain the magnetic field, we first need to simulate a modulation-demodulation scheme as the ones employed in spectropolarimeters like TuMag or SO/PHI. For this purpose, four different modulations have been generated with etc.

2.2.2   Observations simulation.

All the instruments built around the use of an etalon as a wavelength filtering element operate in a very similar way. They scan a spectral line by tuning the etalon (by changing the distance between mirrors and/or modifying the refractive index) to a desired number of wavelengths along the spectral line. At each spectral position, the solar scene is recorded. The measured intensity is approximately given by Eq. (2.1), with the etalon's transmission profile centered at the desired wavelength.

We have carried out two sets of simulations, one with a perfect telecentric configuration, where the incidence is normal, and one with an angle of incidence of the chief ray is $0.5°$. For each of these sets, a simulated observation of the sunspot has been carried out employing 45 wavelengths for the scan of the line. A flat-field observation has also been computed with the same configuration than the one employed for the sunspot observation. For the flat-field observations we have generated an *ideal* flat-field where the average profile computed in quiet-sun was replicated at every pixel of the generated image. One of the primary objectives of these simulations is to assess the effects of cavity errors in telecentric setups. Therefore, we conducted these simulations under two scenarios: one incorporating a cavity map and another assuming a defect-free etalon, which serves as our reference.

Although, in practice, it is not often possible to fully characterize the pre-filter, we assumed it has a rectangular shape centered at the wavelength of the observed spectral line (λ_0) and a width of $2\Delta\lambda$ such that only one order of the etalon passes through. With this consideration, equation (2.12) can be written as follows:

$$I\left(\xi, \eta; \lambda_s\right) = g(\xi, \eta) \int_{\lambda_0 - \Delta\lambda}^{\lambda_0 - \Delta\lambda} \iint O\left(\xi_0, \eta_0; \lambda\right) \mathcal{S}\left(\xi_0, \eta_0; \xi, \eta; \lambda - \lambda_s\right) \mathrm{d}\xi_0 \, \mathrm{d}\eta_0 \mathrm{d}\lambda \ . \quad (2.9)$$
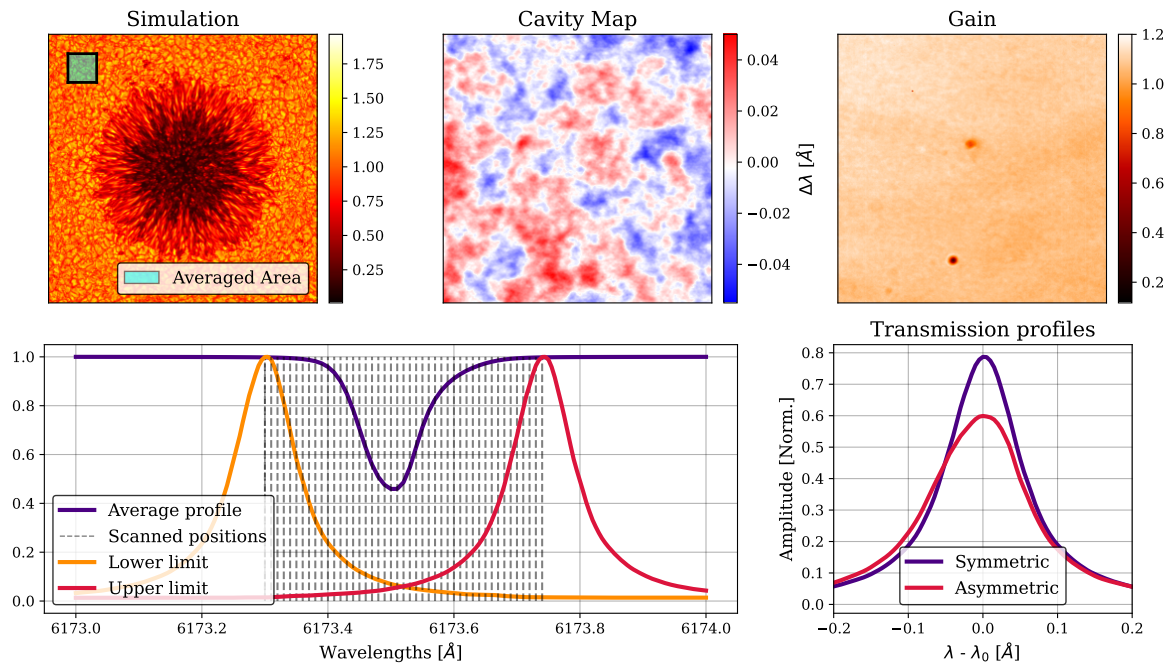
Figure 2.3 Inputs for the simulation of the sunspot observation. The top row shows, from left to right, the continuum of the MHD simulation, the cavity map expressed as the corresponding shift in Å and the gain map. The bottom row shows, again from left to right, a representation of the quiet-sun average profile with all the scanned wavelengths, and the transmission profile of the two different FPI configurations, the symmetric (perfect telecentric) and asymmetric (imperfect telecentric). The parametets employed for the etalon are: $R = 0.892$, $n = 2.3268$, $d = 281\ \mu m$, $f = 60$, $\Theta = 0°$ (symmetric), $\Theta = 0.5°$ (asymmetric).

For every tuned wavelength, the instensity in a given pixel is given by equation (2.9), where the observed object is the sunspot simulation or the generated *ideal* flat-field.

The imaging response of the FPI is computed by solving the integrals in equation (2.2). Given that we will account for the PSF in these simulations, numerical methods are necessary to evaluate the integrals. The computational burden is significant, as the integrals must be evaluated $N^2_{pixel}N_\lambda N_{mods}N_{sets}N_{cavities} > 2 \times 10^8$ times[2] for both sunspot and flat field observations. This extensive computation results in excessively long simulation times. To address this issue, a neural network was developed to reduce the computational time from X to X. The neural network was trained with known solutions to the integrals for a fixed set of etalon parameters, ensuring that its outputs are accurate to within 0.01% for parameters within the training set.

In real-world scenarios, variations in pixel sensitivities (gain) and etalon imperfections (cavity map) are unavoidable. Including the effect of the gain into the simulation is straigghtforward as it only acts as a multiplicative factor that modifies the final intensity. In contrast, the effects of the cavity map are more cumbersome. Pixel-to-pixel variations in etalon defects shift the transmission profile of the FPI and must be accounted for when computing the imaging response. Both the gain and cavity map introduced in the simulations have been selected to resemble the real-case scenario of the SO/PHI instrument. The gain map (Fig. 2.3 top right panel) utilized in the simulations is derived from a flat field of the SO/PHI-HRT instrument, and the cavity map employed (Fig. 2.3 top central panel) is sourced from the cavity map of PHI's etalon.

2.2.3   Flat-field correction.

In principle, flat-field correction is straightforward: first, the measured flat fields are normalized to preserve the spectral line information; second, the observations for all tuned wavelengths are divided by the corresponding normalized flat field. However, in telecentric setups, this process is more challenging because flat-field observations are influenced by cavity errors, which can introduce additional artifacts into the measurements rather than (or in addition to) correcting them.

Figure 2.4 shows the flat-fields observed at the core of the line for the simulations with and wihout cavity and the spectral profiles for a series of pixels. The effect of the cavity map in the flat-field observations is clearly displayed in both representations. In the flat-field itself, higher values of the cavity map appear brighter, as any displacement from the line core to either the blue or the red will result in an increase of the final intensity. In the spectral profiles, the pixels corresponding to higher values of the cavity error show a noticeably shift with respect to the rest position of the line core.

From the normalized profiles, it is also evident that the normalized flats with cavity error will modify the spectral profile of the observations. Nevertheless, in order to correct for the effects of the cavity, the flat-field's spectral profiles cannot be flat as in the case without cavity, since we need to change the spectral information of the observations (shift

---

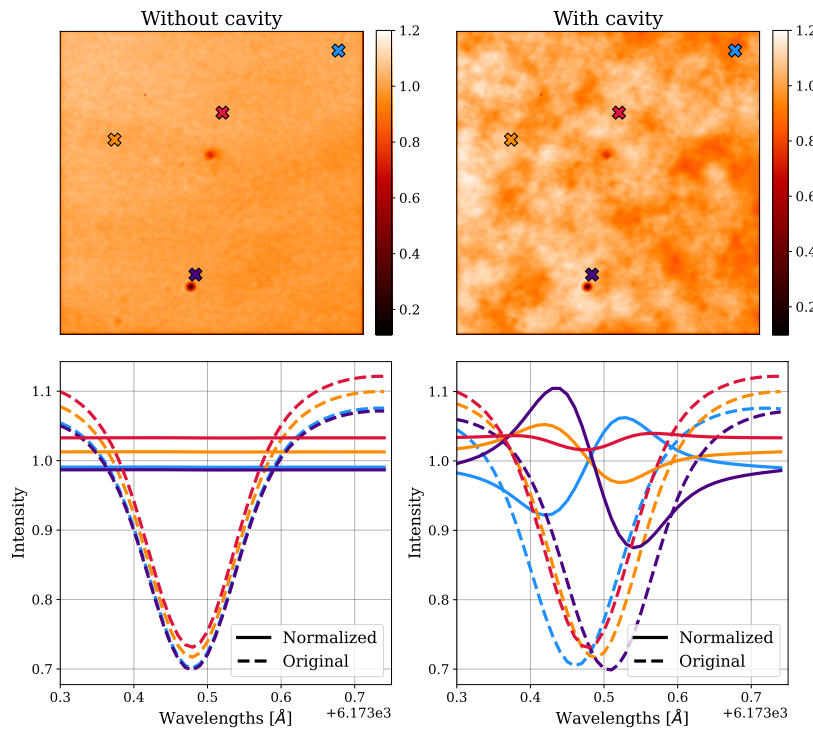[2]$N_{pixels} = 561, N_\lambda = 45, N_{mods} = 2, N_{sets} = 2, N_{cavities} = 2$

Figure 2.4 The top row shows the observed flat-fields at the core of the line for both the simulations without (left) and with (right) cavity. The bottom row shows the spectral profile of the pixels marked with an "X" of the corresponding color, for both scenarios, and before and after the normalization.

the measured profile to the "correct" position). The problem arises when these flat-field not only shift the observed profiles but also (and very noticeably) modify their shape.

The challenges associated with flat-field correction are illustrated in Fig. 2.5, which displays the profiles after flat-field correction for both simulations, with and without the cavity map. Ideally, if the flat-field correction effectively compensates for the cavity errors of the FPI, the profiles from both scenarios should be identical or at least very similar. However, upon comparison, notable differences emerge, particularly for pixels with high cavity map values (light and dark lines). These profiles are not only shifted but also exhibit changes in shape.

This challenge is why some data reduction pipelines adopt a different approach. Instead of using the flat-fields of the corresponding wavelengths, only the continuum flat-field is employed for correction. When the continuum is measured sufficiently far from the spectral line, it remains unaffected by any spectral shift. By using this measurement, one can correct for spurious effects unrelated to spectral shifts, such as pixel sensitivity variations or dust grains. However, this method does not correct for the effects of the cavity.

If the cavity map is thought to be known, the velocity associated with the spectral shift caused by the cavity can be calculated. This "velocity-error" map can then be used to correct the Doppler velocity map derived from the observations that have not been corrected for the cavity map. Theoretically, this approach should address the cavity effects in velocity calculations. Nonetheless, potential impacts of the cavity map on magnetic field calculations remain uncorrected, as the relationship between wavelength shifts and magnetic fields is not as straightforward as in the case of velocity.
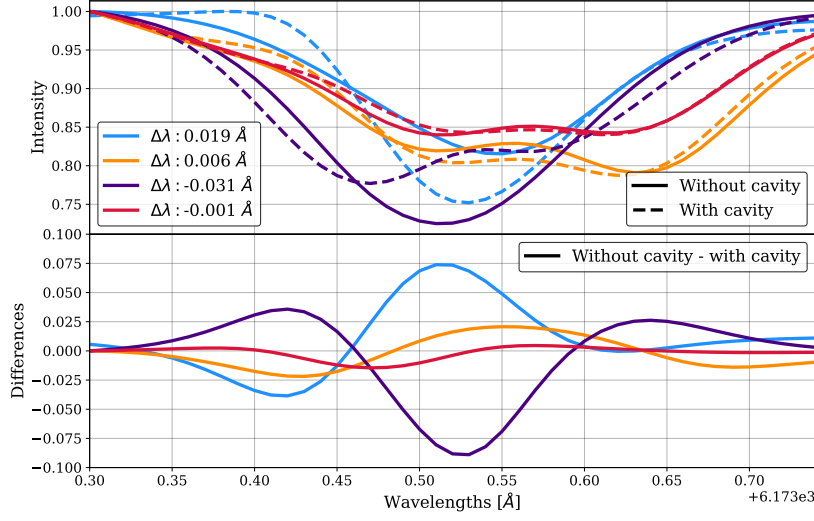
Figure 2.5 The top panel shows four spectral profiles after the flat-field correction for the two scenarios, with and without cavity, and for the symmetric FPI. The selected pixels are the same than in Fig. 2.4, and correspond to different values of the cavity map. The bottom panel shows the difference between the profiles with and witout cavities.

2.2.4   Velocity maps

We begin our analysis by studying the LOS velocities and the errors associated with their computation. These velocities are derived from the spectral shift of each profile relative to the rest position of the spectral line, using the Doppler formula (Eq. (1.7)). Given that this computation relies exclusively on the spectral shift, it is particularly susceptible to errors caused by cavity effects.

According to the center-of-gravity method (Uitenbroek, 2003), the central wavelength of a given spectral profile, λ_{COG}, can be computed from:

$$\lambda_{COG} = \frac{\int \lambda \, (I_{cont} - I) \, d\lambda}{\int (I_{cont} - I) \, d\lambda}. \tag{2.10}$$

Once λ_{COG} has been determined, the spectral shift of the corresponding profile will be given by $\Delta\lambda = \lambda_0 - \lambda_{COG}$.

We have computed the velocities employing the two flat-field correction strategies mentioned in the previos section: the "standard" approach, where each observation is corrected with the flat-field of the corresponding wavelength; and the "continuum" approach, where only the continuum flat-field is employed. Figure 2.6 shows the continuum intensity and the velocity maps obtained for both strategies in the top row.

At first glance, the velocities derived for each approach might look identical, but under closer inspection, some differences arise. In order to highlight these differences and to asses the accuaracy of the obtained velocities we will compare them to the velocity obtained in the scenario where no cavity map was introduced. Figure 2.6 shows this comparisons in the bottom row, along with the cavity map with the umbra and penumbra overplotted to be able to align the error with the cavity.
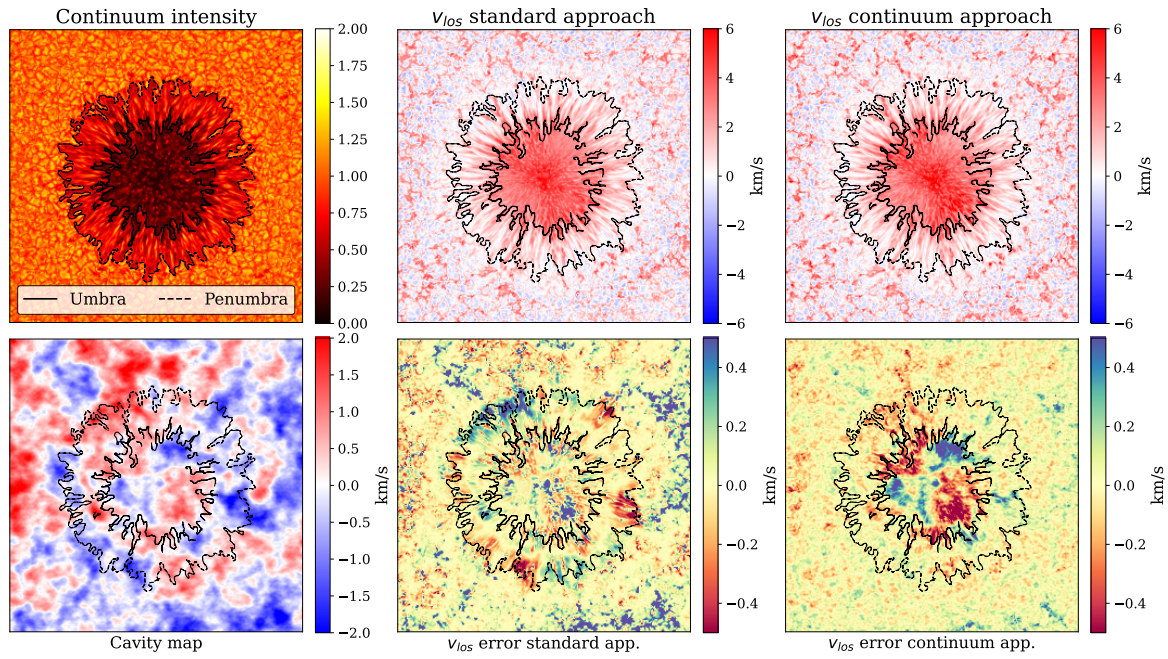
Figure 2.6 The top row shows, from left to right, the observed intensity in the continuum, the LOS velocity for for the standard approach and the LOS velocity for the continuum aproach, all three for the symmetric FPI and belonging to the simulations with cavity map. The bottom row shows, again from left to right, the velocity error associated with the cavity map, the error for the LOS velocity for the standard approach and the error for the LOS velocity of the continuum approach. All representations show the boundaries of the umbra and penumbra for an easier identification of the regions in the velocity and cavity maps.
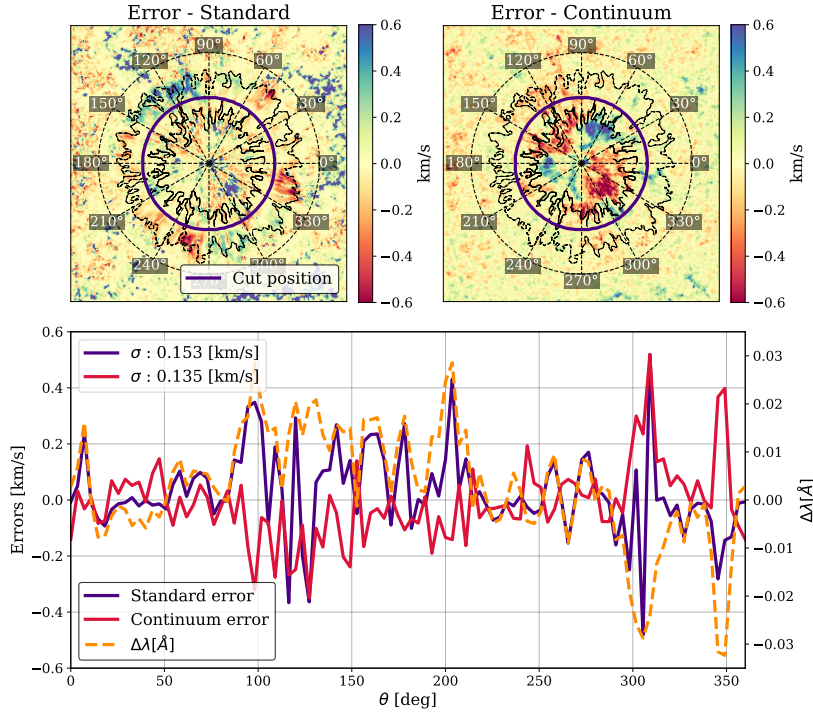
Figure 2.7 The top row shows the velocity error maps for both the standard and continuum approaches, along with the cut position and an overlay of the degrees for easier interpretation of the plotted profiles. The bottom panel shows the velocities along the cut for both aproaches along with the value of the cavity map at the corresponding position.

The error in the velocity computation shows that the effects of the cavity map remain uncorrected in the observations. Both correction approaches exhibit errors with structures corresponding to the cavity map. For the standard correction, this effect is pervasive throughout the field of view (FoV), whereas for the continuum approach, it is primarily concentrated in the umbra, although other regions also exhibit this behavior.

Moreover, the errors are notable, given that regions of the penumbra show errors of around 10%. Errors in the umbra are similarly significant in percentage terms; however, studies of these regions are less frequent due to their low SNR resulting from their inherent darkness. Conversely, extensive research exists on the flows observed in the penumbra (Ref XX??), prompting us to prioritize investigation in this area.

A more quantitative analysis is shown in Fig. 2.7, where the velocity error along a circular path is shown, for both approaches, in addition to the associated spectral shift of the cavity values at identical positions. This representation clearly demonstrates the correlation between the structural features of the cavity map and the velocity error. For both approaches, with a more pronounced effect observed in the standard approach, the absolute value of the error escalates with increasing spectral shifts of the cavity.

It is evident from the previous analyses that the approach of flat-field correction affects the reuslt as differences are observed between correction approaches, but what about the FPI's transmission profile? It is common practice to neglect the assymetric nature of real telecentric mounts in most data reduction pipelines beacuse the possible effects of the assymetries of the profiles are assumed to be negligible.

Figure X depicts the differences in the computed velocities for the symmetric and assymetric FPIs. The main effect of the assymetry is a systematic shift of the profile measure-

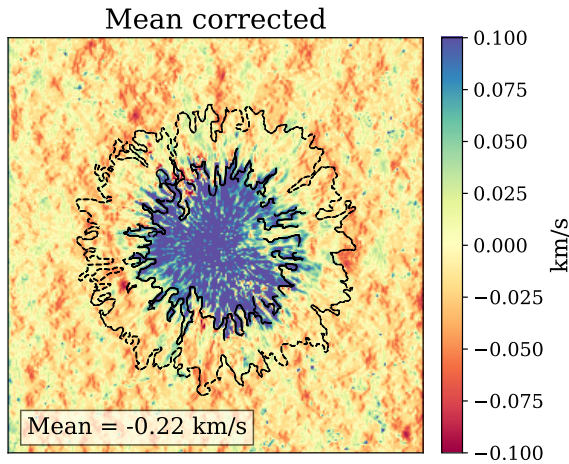Mean corrected

Mean = -0.22 km/s

Figure 2.8 Difference in LOS velocities between the symmetric and assymetric FPIs (symmetric - asymmetric). The mean value of the difference has been substracted for the whole FoV.

ments towards the red wing of the spectral profile, due to its higher transmissivity than its blue counterpart. This shift results in an average difference of around 0.2 km s^{-1} that can be seen over the whole FoV.

This systematic shift can be removed from the velocities computed with the assymetric FPI by substracting the average difference between symmetric and assymetric velocities. The panel XX of figure XX, shows the difference following this correction has been carried out. Despite accounting for the systematic shift, discrepancies are still present, predominantly within the umbra, though they are observed across the entire FoV. The umbra is again more sensible than other regions, displaying the highest error in the whole map, mainly exhibiting a shift towards the BLUE?, for the assymetric scenario. Outside the umbra, differences are smaller, reaching up to 100 ms^{-1}, typically trending towards the red.

The fact that the umbra exhibits different behaviors compared to the rest of the FoV, along with the difference nted between the two types of FPIs, suggests that the amplitude and behavior of these effects are sensitive to the shape of the spectral profile and the FPI's transmission profile.

2.2.5   Magnetic field maps.

It is expected that cavity errors significantly impact velocity calculations, as these are derived solely from the analysis of spectral shifts. However, the effect of these errors on the calculation of the magnetic field is not as straightforward as its determination involves not only the spectroscopy, but also polarization.

To calculate B_{LOS}, we need to determine the circularly polarized component of the light. This requires demodulating the simulated observation using a process analogous to that described in the TuMag pipeline (ref XXX). Once the stokes components have been determined, the LOS strength of the magnetic field is computed using the center-of-gravity method (eq. (1.8)).

Figure 2.9 shows the LOS strength of the magentic field for the simulation with no cavity (the one employed as reference) and the errors in its calculation for both flat-fielding
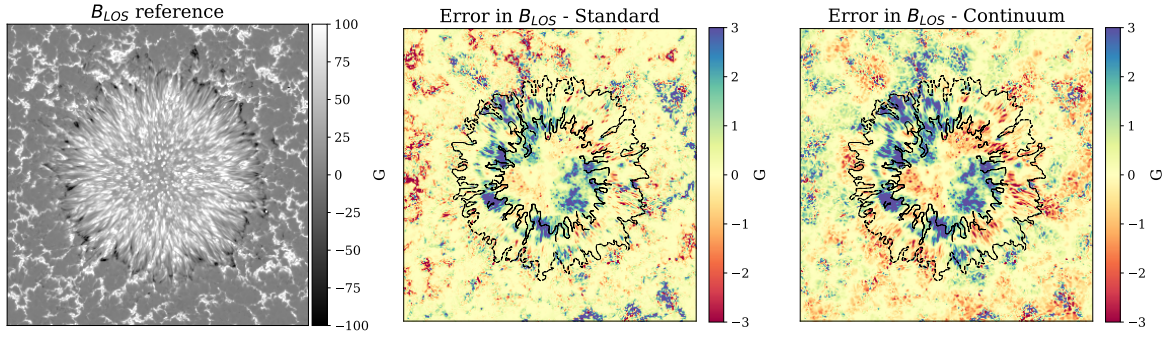
Figure 2.9 From left to right, B_{LOS} for the simulation with no cavity and a symmetric FPI, error in B_{LOS} computation for the standard approach with a symmetric FPI, and error in B_{LOS} computation for the continuum approach with a symmetric FPI.

approaches. In the continuum approach, the structures observed in the error map closely resemble those in the cavity map. This similarity is expected since no correction has been applied to account for the cavity error. While it is possible to compute the velocities associated with the spectral shift caused by the cavity map, this is not feasible for the magnetic field. Consequently, any effect of the cavity remains in the data when using the continuum approach.

As a result, errors in the magnetic field computation appear larger or more prevalent across the entire field of view (FoV) for the continuum approach. Although small, these residuals of the cavity map in the magnetic field map are one of the main problems of employing the continuum apprach in real data.

However, for both correction strategies, the errors remain relatively small, reaching values of approximately 3 G, compared to magnetic field signals of around ±100 G.

2.3   Fitting algorithm

Different approaches have been taken to address these additional corrections. Typically, each instrument has a specific data reduction pipeline where the corrections are carried out taking into account the individual properties of the instruments, hence giving rise to different methods. For example, instruments with a collimated FPI require a specific correction addressing the wavelength blueshift of the profiles due to the variation in the angle of incidence of the incident beam along the field of view (FoV). Meanwhile, for telecentric setups, local inhomogeneities in the flatness of the interferometer's mirrors (cavity errors) are translated into local shifts of the transmission profile. Some pipelines address these deviations by correcting them only at first order through a flat-fielding procedure with no further computations, and some others take additional steps that take into account the specific properties of the instrument. An example of a more detailed calibration pipeline can be found in Schnerr et al. (2011). By using a simplified analytical expression for the etalon transmission profile, Schnerr et al. were able to extract from the flat fields the contribu-

tions caused by the FPI cavity errors and variations in reflectivity for the CRISP instrument, which are then taken into account in the data calibration.

For the first order, this is a good approximation, but since asymmetries in the transmission profiles naturally arise in telecentric instruments (Bailén et al., 2019a), deviations originating from them cannot be fully corrected. Thus, knowledge of the exact shape of the transmission profile is necessary to fully account for these deviations. Scharmer et al. (2013) already allowed asymmetries to be dealt with in the pipeline of the CRISP instrument, but the asymmetries originated from wavelength shifts induced by two distinct etalons, or from an angular dependence along the FoV introduced to approximate the behavior in telecentric setups.

In this work, we aim to further extend and generalize the strategy employed in Schnerr et al. (2011) and Scharmer et al. (2013) by including the exact shape of the transmission profile for the telecentric configuration in the analysis. By doing so, we can fit and take into account the presence of asymmetries in the profile that arise in these setups due to an asymmetric pupil apodization. We have developed a method for deriving the etalon properties from the data in such a way that prior knowledge of the distribution and magnitude of the defects is not needed. We do not make any distinction between defects associated with the mirror's flatness or separation, refraction index, or cavities. This way, we ensure the applicability of the algorithm to all types of FPIs (air and solid). Our technique also differentiates the effects associated with the etalon from other corrections not related to it, such as pixel-to-pixel variations of the gain across the detector. By comparing the theoretical prediction, obtained through the analytical expressions of the transmission profile, with the measured data, we can disentangle the etalon properties from the flat-field observations. In Sect. **??**, we present the analytical expressions for modeling FPIs.

2.3.1   Initial approximations

As an initial approximation, we will disregard the spatial PSF and assume that the spatial dependence can be represented by a Dirac delta function to simplify the equations. Therefore, if we assume that the image response of the FPI follows the expression:

$$S\left(\xi_0, \eta_0; \xi, \eta; \lambda - \lambda_s\right) = \delta(\xi_0 - \xi, \eta_0 - \eta)\Psi(\xi, \eta, \lambda - \lambda_s), \qquad (2.11)$$

equation (2.1) simplifies into:

$$I\left(\xi, \eta; \lambda_s\right) = g(\xi, \eta) \int_0^\infty T(\lambda)O\left(\xi, \eta; \lambda\right) \Psi\left(\xi, \eta; \lambda - \lambda_s\right) d\lambda. \qquad (2.12)$$

The explicit shape of Ψ is different depending on the optical configuration of the instrument, that is, collimated or telecentric.

2.3.2   Simulated observations

We carried out a series of simulations of a spectral line observation in different conditions. We used the Kitt Peak FTS-Spectral-Atlas as the reference (Brault & Neckel, 1987)

and, specifically, the Fe I spectral line at 6173.3 Å. Each observation was composed of N_λ wavelengths, where the measured intensity was recorded. At every wavelength λ_s, the corresponding transmission profile of the etalon Ψ^{λ_s} was computed, and the "observed" intensity $I^{\lambda_s}_{\text{obs},i}$ corresponding to a specific spatial location (ξ, η), represented hereinafter by the pixel i, was calculated using Eq. (??). Additionally, we took into account the presence of additive Gaussian noise. This noise does not necessarily respond to any parameter fluctuation within our analytical expressions or photon noise but comes from any unexpected variations that may not have been modeled in the theoretical scheme.

Additionally, we included the presence of defects arising from irregularities or inhomogeneities on either the cavity thickness d, the refractive index n, or from deviations of the angle of incidence θ. In order to simulate this, we introduced a relative perturbation Δa into the etalon equation that accounts for any local deviation of the value of a with respect to its nominal value. This parameter changes from pixel to pixel differently for the collimated and telecentric configurations. In the former, the profile shifts across the FoV only because of the different incidence angles of the light beam on the etalon. In the latter, local variations of n and/or d are mapped directly onto the detector. We also note that variations in the incidence angle must be considered as well when the degree of telecentrism varies along the detector. Analytically, the parameter a at each i-th pixel is given by $a'_i = a\Delta a_i$, where $a = (2\pi/\lambda)nd\cos\theta$ is constant along the FoV. Note that rewriting the equations for the transmission profiles (sections 2.1.1 and 2.1.2) using this definition of a is straightforward. In collimated configurations, the parameter δ (eq. (2.4)) is simply $2a$. In perfect telecentric configurations, θ is always 0, so the given transmission profile is already expressed in terms of a.

We let $n^{\lambda_s}_i$ be the noise contribution at the i-th pixel and wavelength λ_s. Thus, the observed intensity at that pixel when the etalon is tuned at λ_s, $I^{\lambda_s}_{\text{obs},i}$ is given by

$$I^{\lambda_s}_{\text{obs},i} = g_i \frac{\int_{\lambda_0-\Delta\lambda}^{\lambda_0+\Delta\lambda} O(\lambda)\Psi^{\lambda_s}(\lambda, \Delta a_i)d\lambda}{\int_{\lambda_0-\Delta\lambda}^{\lambda_0+\Delta\lambda} O(\lambda)\Psi^{\lambda_c}(\lambda, \Delta a_i)d\lambda} + n^{\lambda_s}_i, \tag{2.13}$$

with λ_c being the continuum wavelength. From a practical point of view, the integration limits are set in such a way that only a single resonance (or order) of the etalon is included with the limits, thus, acting akin to the sorting pre-filter commented on previously. We note that the denominator strictly corresponds to the intensity at the continuum of the line in the absence of the transmission profile or if the continuum wavelength is far enough from the spectral line. In any other case, the transmission should be taken into account as well to normalize the observations to the local continuum, which is necessary since we work with relative measurements. An example of a spectral line measurement is displayed in Fig. 2.10.

For both the collimated and telecentric configurations, we modeled etalon and gain imperfections over a 100×100 px^2 image. Pixel-to-pixel variations in the sensor efficiency were modeled following a random spatial distribution, as shown in Fig. 2.11 (top panel). Additionally, we included a set of pixels with very low gain values, which represent a group of dead pixels or dust grains.
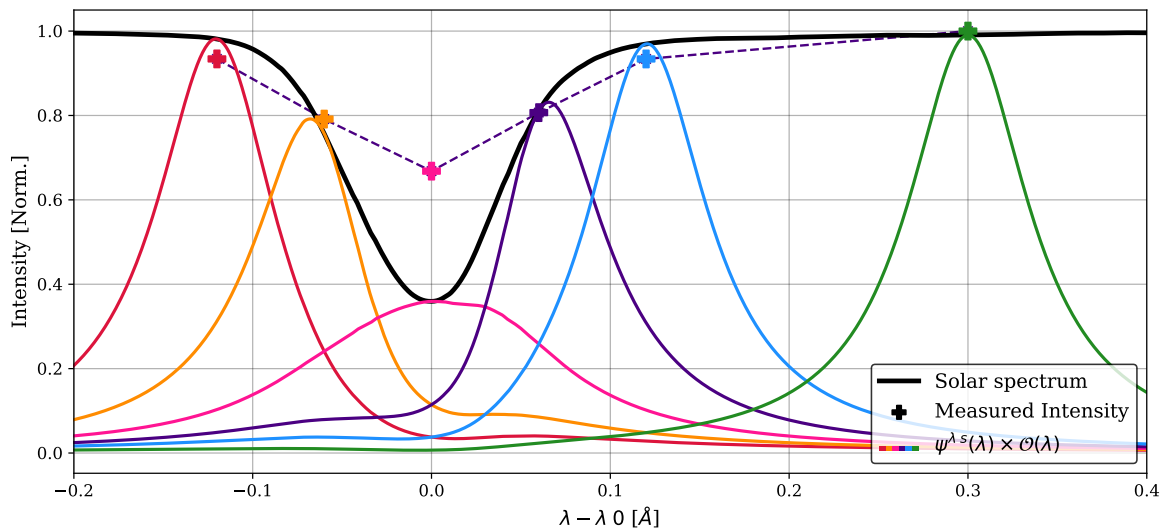
Figure 2.10 Simulated observation of the Fe I spectral line (λ_0 = 6173.3Å) using a collimated mount and a total of N_λ = 6 wavelengths that have been equally distributed along the spectral line, with the exception of the continuum measurement (light blue), which is selected at 300 mÅ from the blue of the line core. The measured intensity is the result of computing the value given by Eq. 2.13 at each wavelength and with g = 1.

We modeled the etalon defects as changes in Δa in such a way that the maximum displacement reaches 3 pm. The spatial distribution of the values of Δa follows an increasing radial distribution, as shown in Fig. 2.11 (bottom panel). Such a spatial distribution coincides with the expected one in collimated etalons due to the change in the incidence angle across the FoV. Telecentric mounts do not exhibit a spatial distribution of their defects such as this, but using the same spatial distribution in the two cases allowed us to compare the performance of the method for both setups in a systematic way. Since Δa accounts for relative perturbations, it is by definition an adimensional parameter. However, to grant it a physical meaning, we express the values of Δa in Å, representing the associated shift of the transmission profile with respect to the original position determined by a.

2.4   Fitting algorithm

We have developed an algorithm able to extract the distribution of the etalon defects and the gain map from data taken by etalon-based instruments, which enables the correction of the two contributions separately. The algorithm works by minimizing a given merit function that depends on the gain and the etalon defects.

In particular, we have defined an error metric, ε^λ, at each tuned wavelength, computed by comparing the measured intensity with the theoretical prediction. If we let $I_{i,\text{obs}}^{\lambda_s}$ be the measured intensity at a given i pixel for an etalon tuned to the wavelength λ_s, the error
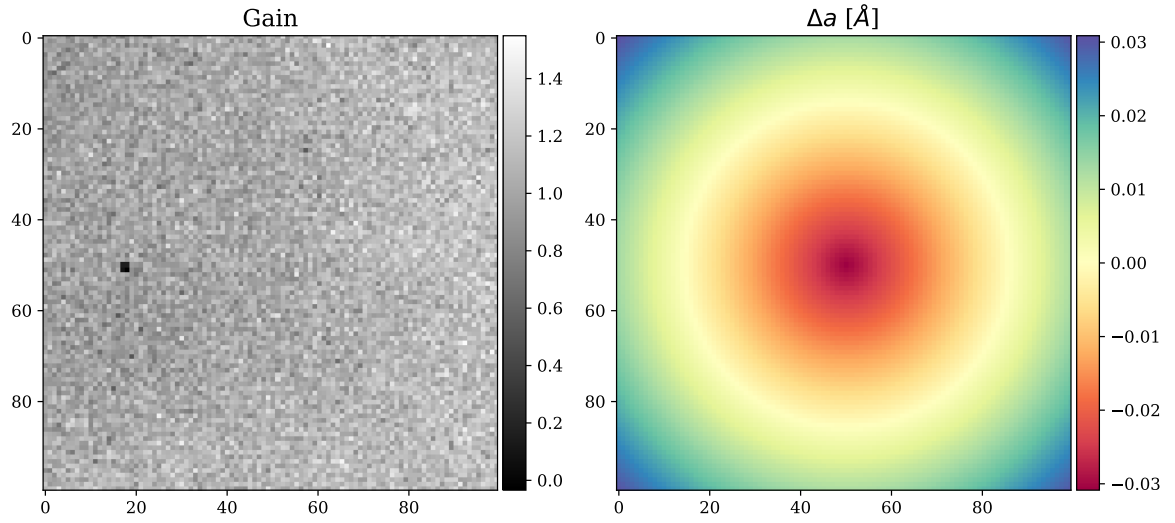
Figure 2.11 Input maps introduced when simulating the observations. The left panel represents the gain generated as white Gaussian noise, with values ranging from 0.8 to 1.2. A dust speck was introduced by creating a group of four pixels with low values of $g = 0.2$ for the gain. The right panel shows the spatial distribution of the defects in the etalon. The distribution follows a radial pattern starting from the center of the FoV. The defects vary from 0 % deviation to up to 5×10^{-4} %, which corresponds to a shift of 3 pm. Both possible directions for the deviations have been considered. The sign of the deviation is negative at the very center, which introduces a redshift, while it is positive at the corners, causing a shift of the profile into the blue.

metric at each wavelength is given by

$$\varepsilon^{\lambda_s}(\Delta a_i, g_i) = I^{\lambda_s}_{i,\text{obs}} - g_i \frac{\int_{\lambda_p}^{\lambda_q} O(\lambda)\Psi^{\lambda_s}(\lambda, \Delta a_i)d\lambda}{\int_{\lambda_p}^{\lambda_q} O(\lambda)\Psi^{\lambda_c}(\lambda, \Delta a_i)d\lambda}. \tag{2.14}$$

The merit function we employed is then the quadratic summation of the error metric over all tuned wavelengths:

$$f(\Delta a_i, g_i) = \sum_{s=0}^{N_\lambda} \left(\varepsilon^{\lambda_s}(\Delta a_i, g_i) \right)^2. \tag{2.15}$$

Both the camera gain and the defects of the etalon change from one pixel to another, which is why we address each pixel independently, but they remain constant at every wavelength. Hence, the transmission profile of the etalon varies at different points of the FoV; but at a given pixel, it is constant at all tuned wavelengths. Therefore, the algorithm is able to better obtain the etalon properties as we increase the number of wavelengths.

Figure 2.12 shows the derivatives of the error metric, Eq. (2.14), as a function of wavelength, that is, before computing the summation over s of the merit function, with respect to the gain, the reflectivity, and Δa. The curve corresponding to the Δa derivative is different from the others, whereas the derivatives of both the gain and the reflectivity exhibit similar shapes. Hence, variations in either the reflectivity or the gain introduce similar changes in the merit function, which can produce a trade-off between these two parameters, especially when the spectral line is sampled in only a few points. Given that discrepancies arising from errors in reflectivity are assimilated by gain maps, we did not take into account reflectivity errors when computing our simulations, as they have no impact on cavity map calculations.

A few key aspects arise when analyzing the merit function and its applicability on real data. The first point to bear in mind is that the shape of the object, $O(\lambda)$, is not known a priory. Therefore, we needed to provide a guess for it. The method works by assuming that differences between the prediction and the observation are caused exclusively by the etalon defects or the gain. If the object used during the fitting process differs considerably from the real one, the prediction and observation will have differences that will erroneously be identified as etalon defects or gain variations. This is the main source of errors for the method when applied to real data. Two approaches can be followed in order to address this issue. The first one consists of assuming the solar atlas profile as the object. This is a good approximation, provided the data to which the algorithm is applied to lack information about solar structure, either because they are observations of long integration times of the quiet sun or produced by averaging several quiet sun observations (flat fields). If this condition cannot be met, this approach is not valid. The second approach involves deriving an approximated object from the data themselves by deconvolving the mean profile of the observation with the etalon's transmission profile. This approach can account for any difference the real object may have with the solar atlas and thus has a greater resemblance to
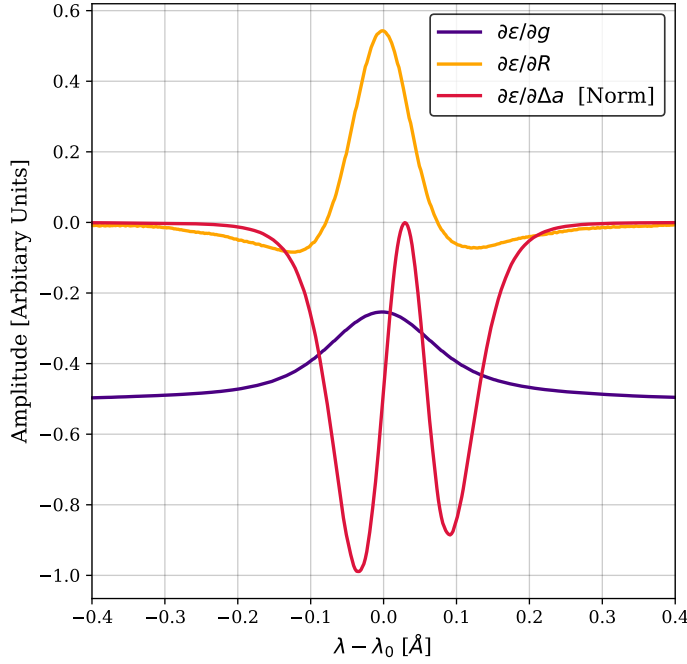
Figure 2.12 Derivatives of the error metric as a function of wavelength. The derivative with respect to Δa has been normalized in order to fit the three curves in the same plot.

the real object. Nevertheless, the process of deconvolving is prone to errors when the sampling is insufficient and can introduce additional noise into the problem. We have tested both approaches to compare their performances on different scenarios in order to assess when to use one or the other.

We employed Newton's method to minimize the merit function, Eq. (2.15), as it has been proven to quickly converge (in five iterations or fewer, usually). The method begins by assuming an initial guess for the gain g_j and Δa_j parameters. Then, provided the initial guess is sufficiently close to the solution and that the merit function is continuous and differentiable, the gain g_j and Δa_j encoded in the vector, $\mathbf{x}_j$, can be updated iteratively at each iteration, j, as

$$\mathbf{x}_{j+1} = \mathbf{x}_j - \mathcal{H}^{-1}\mathcal{J}^T f(\mathbf{x}_j)\,, \tag{2.16}$$

where $\mathcal{H}$ and $\mathcal{J}$ are the Hessian and Jacobian matrices of the merit function f, respectively, calculated for $\mathbf{x}_j = [g_j, \Delta a_j]^T$, and T stands for the transpose. Hence, the transmission profile of the etalon and its derivatives have to be computed for every wavelength and every pixel at each iteration. This can be computationally costly, especially when using imperfect telecentric configurations, where numerical integrals are involved. All derivatives needed for the algorithm are calculated analytically, except when simulating imperfect telecentrism. A detailed formulation of these derivatives is provided in the appendix.

Regarding the object $O(\lambda)$, if we assume it is given by the solar atlas, no additional computations are needed. However, when using the deconvolution approach, the object has to be calculated in each iteration. In this case, the algorithm works as follows: First, we compute the average profile across the whole FoV, and we force the continuum intensity to be the same on both sides of the spectral range to reduce the boundary effects of the
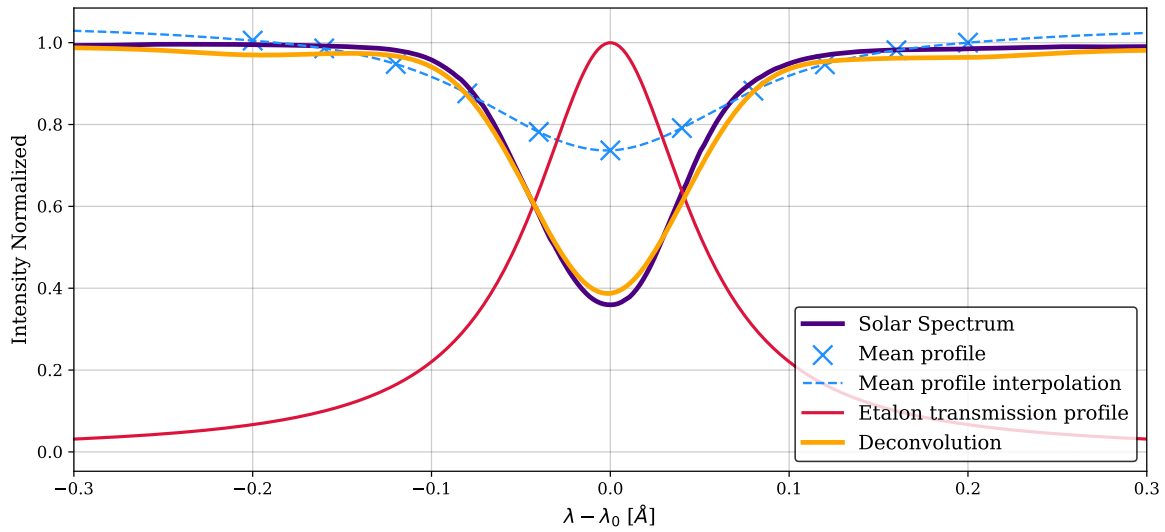
Figure 2.13 Deconvolution of the object with a measurement of the Fe I spectral line using $N_\lambda = 9$. All points of the FoV have been used to compute the average profiles (blue crosses). The deconvolution (orange) is the result of deconvolving the mean profile interpolation (dashed line) with the displayed etalon transmission profile (red).

deconvolution. This step is only necessary in case the spectral line is sampled in only a few positions, as is the case of the SO/PHI, IMaX, or TuMag instruments, where only a continuum point, either at the red or the blue side of the spectrum, is recorded. Both the object and transmission profile require a good spectral sampling to accurately compute the integrals of Eq. (2.14). Second, a cubic spline interpolation is applied to the generated average profile to artificially improve the spectral sampling, if necessary. Finally, the interpolated profile is then deconvolved by means of a Wiener filter with the etalon's transmission profile. The result of this deconvolution is the object, $O(\lambda)$, used in the minimization algorithm. The deconvolution of the object is done every time the etalon defects are updated in order to improve the resemblance of the deconvolved object to the real one. Figure 2.13 shows an example of this process in a simulated observation using nine scanned points and a collimated configuration. The deconvolution manages to reproduce the original signal, with only some minor differences in the line core and the beginning of the wings.

2.4.1 Test scenarios and results

The aim of the simulations carried out in this section was to characterize the role of the noise $\delta_i^{\lambda_s}$, the spectral sampling, the selection of the object $O(\lambda)$, and the accuracy of the method for both the collimated and telecentric configurations. All simulations were run for different choices of the number of scanned wavelengths, ranging from $N_\lambda = 5$ to $N_\lambda = 21$.
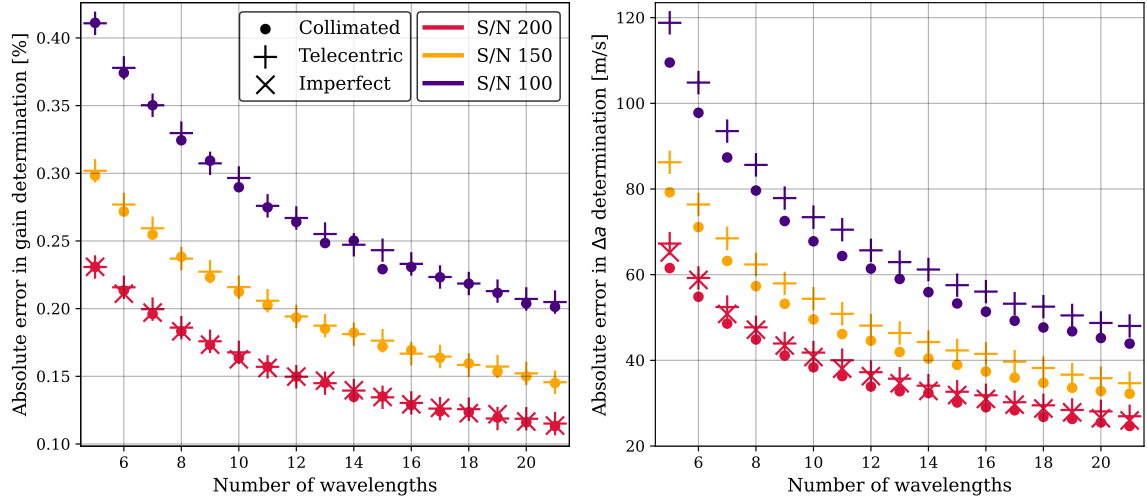
Figure 2.14 Absolute errors of the gain (left) and etalon defect (right) derivations averaged over all the FoV. The number of wavelengths corresponds to the parameter N_λ of wavelengths used to scan the profile.

2.4.1.1   Impact of the noise level

We first assumed that the spectrum of the observed object is given by the solar atlas. This way, all errors in the derivation of the gain and etalon defects only come from the noise introduced into the measurement. We refer to this as the "ideal case." Since we were combining different measurements taken at different wavelengths, we considered a worst-case scenario and simulated three different signal-to-noise ratios: 100, 150, and 200.

We restricted imperfections in the telecentrism to arise only for one scenario, S/N = 200, since simulating imperfections requires a high computational effort due to the lack of a theoretical expression for both the transmission profile and its derivatives. We also assumed that the degree of telecentrism (0.3°) is known in this case.

Figure 2.14 shows the average absolute error in g (left panel) and in Δa (right panel) over the whole FoV as a function of the wavelength sampling, N_λ. The error in g is expressed as a percentage of its real value. Errors in Δa are given in meters per second since they are mostly responsible for shifting the profile. Errors in Δa can be translated into velocity errors by computing the doppler velocity (Eq. (1.7)) associated to the spectral shift of the transmission ppeak produce by the error in Δa. Figure 2.14 shows the average absolute error in g (left panel) and in Δa (right panel) over the whole FoV as a function of the wavelength sampling, N_λ. The error in g is expressed as a percentage of its real value. Errors in Δa are given in meters per second since they are mostly responsible for shifting the profile. Errors in Δa can be translated into velocity errors by computing the doppler velocity (Eq. (1.7)) associated to the spectral shift of the transmission ppeak produce by the error in Δa.

All the scenarios exhibit a similar behavior as far as their dependence on the spectral sampling is concerned, namely, the absolute errors decrease monotonically when the

wavelength sampling increases. The reason for this is simply that a larger number of wavelength samples increases the amount of available information that the algorithm can use, thus making the fitting for g and Δa more precise. These results highlight the importance of properly sampling the targeted spectral line. A modest sampling of only $N_\lambda = 5$ can produce errors as large as 120 ms^{-1} in the worst-case scenario (S/N = 100).

The noise level also plays an important role in the accuracy of the results. Scenarios with a lower S/N always have larger errors, for a given N_λ, in both the gain and Δa computations. The difference in the performance of the algorithm due to the noise also changes with the spectral sampling; scenarios with a poor spectral sampling suffer from larger differences in the accuracy between the different S/N (50 ms^{-1} for $N_\lambda = 5$ between S/N = 200 and S/N = 100) than those with higher samplings (35 ms^{-1} for $N_\lambda = 21$).

The optical configuration of the etalon has a very small impact on the accuracy of the algorithm. Results for the three setups are very similar, particularly in the gain calculation, for which the results are almost identical for all configurations. Retrieval of Δa is slightly better for the collimated mount, though.

Figure 2.15 shows the spatial distribution of the errors in the retrieval of Δa for different choices of N_λ. There are no signs of a radial distribution in the maps shown in the figure, contrary to the actual distribution of the Δa parameter, as shown in Fig. **??**, bottom panel. This means that the precision of the method is similar no matter the amplitude of the defects, that is, we achieve the same accuracy in the retrieval of defects associated with shifts of 3 pm ($\sim 1450 \text{ ms}^{-1}$, near the corners of our FoV), which correspond to cavity errors of around 1.5 nm or incidence angles of approximately 0.4 degrees, and in the retrieval of regions where no defect is present (radius of 20 pixels from the center of the FoV approximately). Instead of a radial distribution, the errors follow a Gaussian-like distribution (shown at the bottom panels in 2.15) similar to the one followed by the noise contribution.

The standard deviation of the errors for both the gain and Δa computations are also reduced with an increase in spectral sampling. The last row of Fig. 2.15 displays the error distributions in the calculation of Δa for the three optical configurations and different spectral samplings. These results illustrate how the three configurations yield practically identical results and how the distribution narrows as N_λ increases, thereby improving the results. Specifically, the standard deviation decreases from 50 ms^{-1} for $N_\lambda = 5$ to 20 ms^{-1} for $N_\lambda = 21$. In the case of the gain determination, the standard deviation ranges between 0.2 % and 0.1% for the scenarios with the poorest and highest spectral sampling, respectively.

2.4.1.2 Impact of the object approximation

To infer the error of the algorithm when the object is unknown, we compared the performance of the ideal case, that is, when the object used to generate the observations is known, with the one achieved when deconvolving the object from the data. Only the collimated setup was simulated in order to focus exclusively on the errors introduced by the deconvolution. The data has been degraded by Gaussian noise with an S/N = 200 in both scenarios.

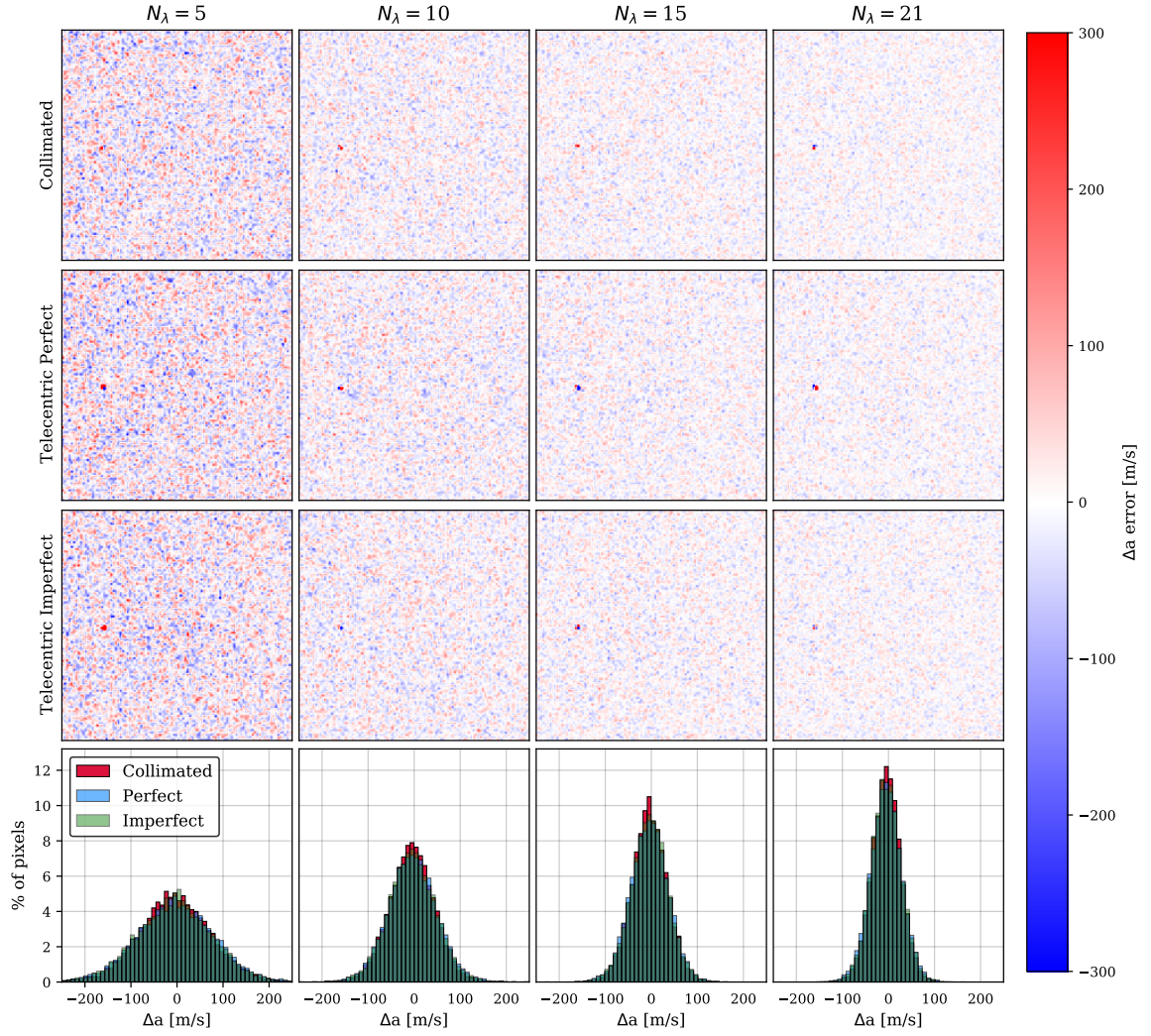Figure 2.16 shows the results for the two approaches. Interestingly, the error in the gain

Figure 2.15 Distribution of the errors in the Δa computation for the three configurations (first three rows) and different spectral samplings (columns). In the bottom panels of each column, the error distribution for the corresponding spectral sampling is shown for the three configurations.
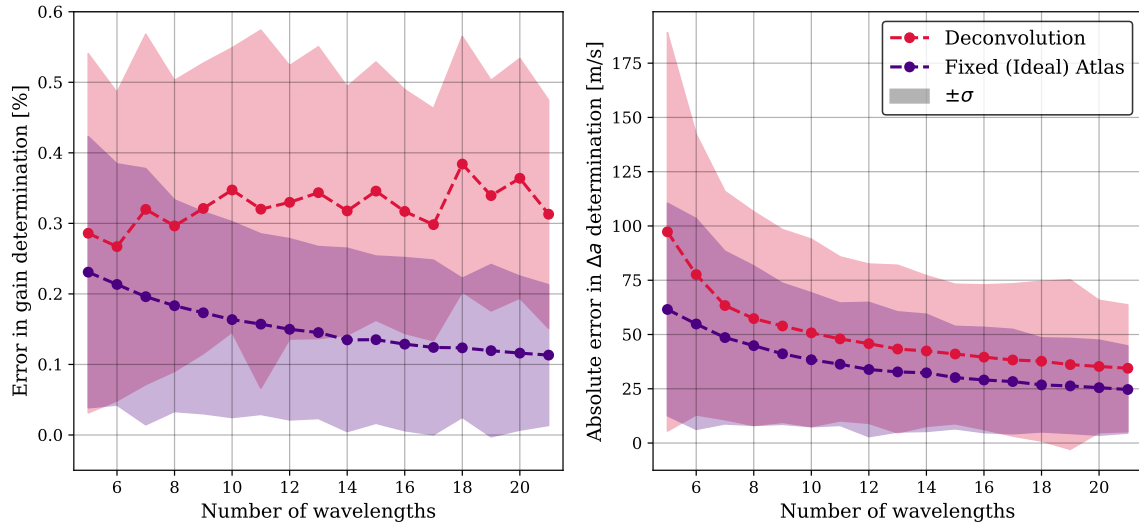
Figure 2.16 Errors in gain determination and etalon properties averaged over all the FoV with a signal-to-noise ratio of 200 and a collimated configuration.

for the deconvolution approach does not decrease with a larger number of wavelengths, unlike the ideal case. Nevertheless, the average error of the calculation is below 0.4 %, with a dispersion (1 σ) of ± 0.3 %. The deconvolution approach is prone to higher errors when deriving the gain due to the normalization of the profiles. The reason for this is two-fold. first, if the continuum is far enough from the spectral line, the normalization is strictly the integral over the transmission profile because the object is flat along the integration interval. However, this is not strictly true since the wings of the transmission profile can reach the spectral line (see Fig. ??), hence modifying the normalization of the profile when the object changes at each iteration. Second, should the continuum intensity of the derived object vary with respect to its real value due to the deconvolution process (e.g., due to boundary effects), there will be a shift in the intensity of the whole profile induced by the normalization process. These two effects seem to dominate the accuracy on the gain determination, regardless of the chosen sampling.

For Δa, the performance of the method is slightly worse than for the ideal case when using the deconvolution approach. Unlike the gain determination, errors in the Δa derivation show a strong dependence on the spectral sampling. Differences between both approaches range from 10 ms^{-1} to 40 ms^{-1} and increase with decreasing N_λ. The sensitivity with N_λ is especially high up to $N_\lambda = 8$. A modest increase of N_λ from five to six improves the determination of $\Delta a \sim 20$ ms^{-1}, whereas at better spectral samplings, the difference between each simulation decreases more slowly, without any relevant improvement as the sampling increases. In any case, differences are all well within ±1σ.
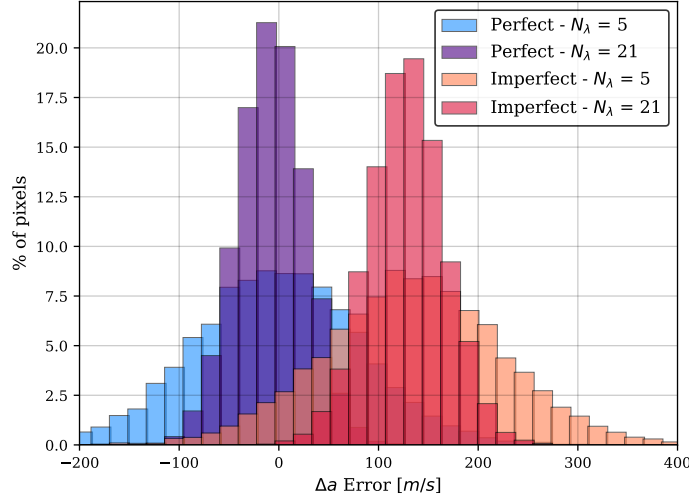
Figure 2.17 Distribution of the errors in the determination of Δa for the crossover scenarios (different configuration in the observation generation and minimization algorithm) for both perfect and imperfect configurations. Only results for the two extreme spectral samplings ($N_\lambda = 5$ and $N_\lambda = 21$) are shown.

2.4.2 The crossover case

The fact that the sensitivity of the model to the gain and to the Δa parameters are different guarantees (to some extent) that the parameters can be separated from each other. The treatment of the problem is very different between etalon configurations, and therefore full knowledge of the setup is critical. However, this is not always feasible due to the unavoidable presence of errors, misalignment, and imperfections on the instrument. Approximations to describe the optical setup are also common in the pipeline of an FPI instrument because they reduce computational efforts. For instance, telecentric mounts are usually simplified as collimated setups, as the f-numbers employed in solar instruments are usually very large. Imperfections of telecentrism are commonly neglected, too. In this section, we analyze the impact of assuming an incorrect etalon mounting. To do so, we repeated the previous exercise, starting from a perfect and imperfect telecentric configuration but assuming that the transmission profile shape corresponds to a collimated one.

In this exercise, we assumed that we have an instrument with an FPI in a telecentric mount, as in the previous sections, in both perfect and imperfect configurations and an S/N = 200. We also considered that the object is given by the spectral solar atlas. The shift of the perfect telecentric transmission profile with respect to the collimated one was corrected using Eq.52 from Bailén et al. (2019a) to avoid the emergence of spurious velocity signals. Imperfections in the telecentrism shift the profile more. This additional displacement was left uncorrected intentionally so we could study its effects.

Figure 2.17 shows the error distributions for Δa when the model assumes a collimated configuration for $N_\lambda = 5$ and $N_\lambda = 21$ and for both perfect and imperfect configurations. The amplitude and dispersion of the error distributions are very similar for the two mounts and are comparable to the results obtained in the ideal case (Fig. 2.15, bottom panel). The main difference between the perfect and imperfect scenarios is a shift of 130 ms^{-1} for the reason mentioned above. We note that this shift can easily be accounted for since it is a known and measurable effect.

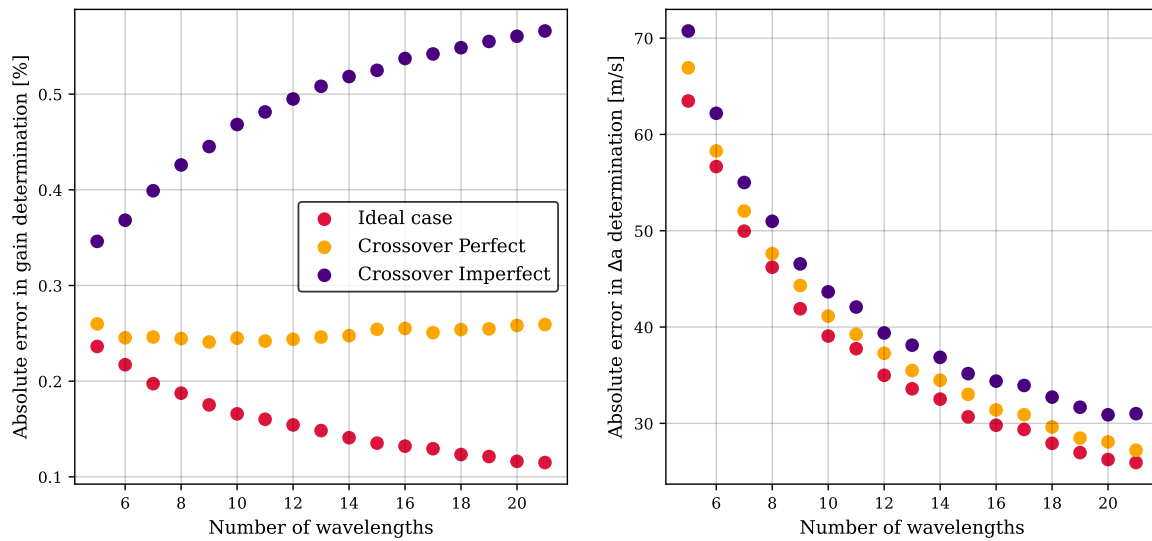The similarity in the error distributions for the calculation of Δa in the two scenarios

Figure 2.18 Average errors of the gain (left) and etalon defect (right) calculations over all the FoV for the two crossover cases and the standard case (also shown in Fig. 2.14 as the collimated case with S/N = 200) for reference. All Δa errors have been computed by correcting differential offsets of the transmission profile between the different mounts.

demonstrates that the error incurred when assuming a collimated etalon does not significantly impact the determination of the cavity maps of the etalon. This is because changes in Δa mostly induce a shift of the transmission peak by an equal amount in both cases.

We note, however, that the amplitude, width, and shape of the transmission profile differ significantly between the telecentric and collimated configurations, leading to an expected higher error in gain calculation. Figure 2.18 shows the absolute errors in gain and Δa calculations for both crossover scenarios and the ideal case after correcting the wavelength shift between the different mounts. For Δ_a, the performance of the method is very similar in the three setups, as also observed earlier. This behavior is nevertheless anticipated since the properties selected for simulating the imperfect etalon were chosen to mirror those of the SO-PHI etalon, which were adjusted to closely resemble the behavior of a collimated etalon to the greatest extent possible.

The differences are larger for the gain determination. Not only are the errors higher in the crossover cases, but the trend is entirely different. Instead of decreasing when increasing the number of wavelengths, gain errors remain the same for the perfect case and increase with the number of samples for the imperfect case. Similar to the deconvolution case (Fig. 2.16), the difference between transmission profiles introduces an error in the normalization process that systematically affects the rest of the measurements. This effect becomes more pronounced as the number of wavelengths increases, given that this error is introduced more frequently, and it is even more prominent in the imperfect case, as not only are the profiles different in this scenario, but they are also asymmetric. This asymmetry results in an imbalance in the measurement of the profile, as one wing of the spectral line has a higher transmissivity and is observed with greater intensity than the other.

Our results suggest that assuming an etalon in a collimated configuration for instruments with telecentric mounts can be a good first-order approximation for cavity map calculations, provided that the level of asymmetry of the transmission profile is known. However, achieving an accurate knowledge of the degree of telecentrism is often challenging in real instruments, as it usually varies across the FoV. Meanwhile, the results highlight that this approximation leads to a considerable increase in the error in the gain determination, which increases when increasing the spectral sampling. This contrasts with the standard philosophy of solar instrumentation, which requires a high number of points to better scan the spectral line.

CHAPTER 3

SUMMARY AND CONCLUSIONS

The conclusions are …

Appendix A

Profile derivatvies

Bibliography

Bailén, F. J., Orozco Suárez, D., & del Toro Iniesta, J. Fabry-pérot etalons in solar astronomy. a review. *Astrophysics and Space Science* **368**, 55 (2023).

Bailén, F. J., Suárez, D. O., & del Toro Iniesta, J. On fabry–pérot etalon-based instruments. i. the isotropic case. *The Astrophysical Journal Supplement Series* **241**, 9 (2019).

Bailén, F. J., Suárez, D. O., & del Toro Iniesta, J. On fabry–pérot etalon-based instruments. ii. the anisotropic (birefringent) case. *The Astrophysical Journal Supplement Series* **242**, 21 (2019).

Bailén, F. J., Suárez, D. O., & del Toro Iniesta, J. On fabry–pérot etalon-based instruments. iii. instrument applications. *The Astrophysical Journal Supplement Series* **246**, 17 (2020).

Bailén, F. J., Suárez, D. O., & del Toro Iniesta, J. On fabry–pérot etalon-based instruments. iv. analytical formulation of telecentric etalons. *The Astrophysical Journal Supplement Series* **254**, 18 (2021).

Barthol, P., Gandorfer, A., Solanki, S. K., et al. The sunrise mission. *Solar Physics* **268**, 1 (2011).

Beckers, J. On the effect of narrow-band filters on the diffraction limited resolution of astronomical telescopes. *Astronomy and Astrophysics Supplement Series* **129**, 191 (1998).

Bianda, M., Solanki, S., & Stenflo, J. Hanle depolarisation in the solar chromosphere. *Astronomy and Astrophysics, v. 331, p. 760-770 (1998)* **331**, 760 (1998).

Brault, J., & Neckel, H. Spectral atlas of solar absolute disk-averaged and disk-center intensity from 3290 to 12510 å. *unpublished (tape-copy from KIS IDL library)* (1987).

Cavallini, F. Ibis: a new post-focus instrument for solar imaging spectroscopy. *Solar Physics* **236**, 415 (2006).

del Toro Iniesta, J. C. (2003), Introduction to spectropolarimetry (Cambridge university press).

del Toro Iniesta, J. C., & Ruiz Cobo, B. Inversion of the radiative transfer equation for polarized light. *Living Reviews in Solar Physics* **13**, 4 (2016).

Evershed, J. Radial movement in sunspots (1909).

Gonsalves, R. A. Phase retrieval and diversity in adaptive optics. *Optical Engineering* **21**, 829 (1982).

Kentischer, T., Schmidt, W., Sigwarth, M., & Uexkuell, M. Tesos, a double fabry-perot instrument for solar spectroscopy. *Astronomy and Astrophysics, v. 340, p. 569-578 (1998)* **340**, 569 (1998).

Martínez Pillet, V., Del Toro Iniesta, J., Álvarez-Herrero, A., et al. The imaging magnetograph experiment (imax) for the sunrise balloon-borne solar observatory. *Solar Physics* **268**, 57 (2011).

Müller, D., Cyr, O. S., Zouganelis, I., et al. The solar orbiter mission-science overview. *Astronomy & Astrophysics* **642**, A1 (2020).

Noda, C. Q., Ramos, A. A., Suárez, D. O., & Cobo, B. R. Spatial deconvolution of spectropolarimetric data: an application to quiet sun magnetic elements. *Astronomy & Astrophysics* **579**, A3 (2015).

Noda, C. Q., Schlichenmaier, R., Rubio, L. B., et al. The european solar telescope. *Astronomy & Astrophysics* **666**, A21 (2022).

Puschmann, K. G., Denker, C. J., Balthasar, H., et al. Gregor fabry-pérot interferometer and its companion the blue imaging solar spectrometer. *Optical Engineering* **52**, 081606 (2013).

Rimmele, T. R., Warner, M., Keil, S. L., et al. The daniel k. inouye solar telescope–observatory overview. *Solar Physics* **295**, 1 (2020).

Scharmer, G. Comments on the optimization of high resolution fabry-pérot filtergraphs. *Astronomy & Astrophysics* **447**, 1111 (2006).

Scharmer, G., & Spruit, H. Magnetostatic penumbra models with field-free gaps. *Astronomy & Astrophysics* **460**, 605 (2006).

Scharmer, G. B., de la Cruz Rodriguez, J., Sütterlin, P., & Henriques, V. M. Opposite polarity field with convective downflow and its relation to magnetic spines in a sunspot penumbra. *Astronomy & Astrophysics* **553**, A63 (2013).

Scharmer, G. B., Narayan, G., Hillberg, T., et al. Crisp spectropolarimetric imaging of penumbral fine structure. *The Astrophysical Journal* **689**, L69 (2008).

Schlichenmaier, R., Jahn, K., & Schmidt, H. Magnetic flux tubes evolving in sunspots. a model for the penumbral finestructure and the evershed effect. *arXiv preprint astro-ph/9807036* (1998).

Schmidt, W., Von der Lühe, O., Volkmer, R., et al. (2012), The 1.5 meter solar telescope gregor, Wiley Online Library.

Schmidt, W., Schubert, M., Ellwarth, M., et al. End-to-end simulations of the visible tunable filter for the daniel k. inouye solar telescope. *Ground-based and airborne instrumentation for astronomy VI*, SPIE, 1473–1483 (2016).

Schnerr, R., de la Cruz Rodriguez, J., & van Noort, M. Stokes imaging polarimetry using image restoration: a calibration strategy for fabry-pérot based instruments. *Astronomy & Astrophysics* **534**, A45 (2011).

Solanki, S., & Montavon, C. Uncombed fields as the source of the broad-band circular polarization of sunspots. *Astronomy and Astrophysics, Vol. 275, p. 283 (1993)* **275**, 283 (1993).

Solanki, S., Riethmüller, T., Barthol, P., et al. The second flight of the sunrise balloon-borne solar observatory: overview of instrument updates, the flight, the data, and first results. *The Astrophysical Journal Supplement Series* **229**, 2 (2017).

Solanki, S. K., del Toro Iniesta, J., Woch, J., et al. The polarimetric and helioseismic imager on solar orbiter. *Astronomy & Astrophysics* **642**, A11 (2020).

Spruit, H., & Scharmer, G. Fine structure, magnetic field and heating of sunspot penumbrae. *Astronomy & Astrophysics* **447**, 343 (2006).

Stokes, G. G. On the composition and resolution of streams of polarized light from different sources. *Transactions of the Cambridge Philosophical Society* **9**, 399 (1851).

Uitenbroek, H. The accuracy of the center-of-gravity method for measuring velocity and magnetic field strength in the solar photosphere. *The Astrophysical Journal* **592**, 1225 (2003).

van Noort, M. Image restoration of solar spectra. *Astronomy & Astrophysics* **608**, A76 (2017).

Van Noort, M., Der Voort, L. R. V., & Löfdahl, M. G. Solar image restoration by use of multi-frame blind de-convolution with multiple objects and phase diversity. *Solar Physics* **228**, 191 (2005).

```
 1  one inch + \hoffset        2  one inch + \voffset
 3  \oddsidemargin = -1pt      4  \topmargin = -7pt
 5  \headheight = 14pt         6  \headsep = 19pt
 7  \textheight = 631pt        8  \textwidth = 441pt
 9  \marginparsep = 7pt       10  \marginparwidth = 88pt
11  \footskip = 30pt              \marginparpush = 7pt (not shown)
    \hoffset = 0pt                \voffset = 0pt
    \paperwidth = 597pt           \paperheight = 845pt
```

```
1  one inch + \hoffset         2  one inch + \voffset
3  \evensidemargin = 13pt      4  \topmargin = -7pt
5  \headheight = 14pt          6  \headsep = 19pt
7  \textheight = 631pt         8  \textwidth = 441pt
9  \marginparsep = 7pt        10  \marginparwidth = 88pt
11 \footskip = 30pt               \marginparpush = 7pt (not shown)
   \hoffset = 0pt                 \voffset = 0pt
   \paperwidth = 597pt            \paperheight = 845pt
```